Astrophysically Motivated Bulge-Disk Decompositions of SDSS Galaxies

C. N. Lackner[1]⋆ and J. E. Gunn[1]

[1]*Department of Astrophysical Sciences, Princeton University, Princeton, NJ 08544*

5 January 2012

ABSTRACT

We present a set of bulge-disk decompositions for a sample of $71,825$ SDSS main-sample galaxies in the redshift range $0.003 < z < 0.05$. We have fit each galaxy with either a de Vaucouleurs ('classical') or an exponential ('pseudo-') bulge and an exponential disk. Two dimensional Sérsic fits are performed when the 2-component fits are not statistically significant or when the fits are poor, even in the presence of high signal-to-noise. We study the robustness of our 2-component fits by studying a bright subsample of galaxies and we study the systematics of these fits with decreasing resolution and S/N. Only 30% of our sample have been fit with two-component fits in which both components are non-zero. The $g - r$ and $g - i$ colours of each component for the two-component models are determined using linear templates derived from the r-band model. We attempt a physical classification of types of fits into disk galaxies, pseudo-bulges, classical bulges, and ellipticals. Our classification of galaxies agrees well with previous large B+D decomposed samples. Using our galaxy classifications, we find that Petrosian concentration is a good indicator of B/T, while overall Sérsic index is not. Additionally, we find that the majority of green valley galaxies are bulge+disk galaxies. Furthermore, in the transition from green to red B+D galaxies, the total galaxy colour is most strongly correlated with the disk colour.

Key words: galaxies: bulges – galaxies: structure – galaxies: evolution – galaxies: photometry.

1 INTRODUCTION

The division of galaxies into spirals and ellipticals and the identification of the central bulges of spirals with ellipticals is very old (Hubble 1936; de Vaucouleurs 1959; Sandage 1961). Reasonably successful quantitative attempts to fit galaxies with elliptical-like bulges and exponential disks (de Vaucouleurs 1948, 1959; Freeman 1970) are almost as old as the availability of imaging detectors (Kent 1985, 1986; Capaccioli et al. 1987). It is not yet clear what evolutionary forces give rise to the two components nor is it clear quantitatively how general the division of bulge and disk is. For example, it has long been recognized that low-luminosity star-forming systems often have no bright central structure (bulge) at all. More recently, it has been recognized that the bright central regions of (particularly) late-type spirals are often *not* 'classical' de Vaucouleurs-like bulges, but flattened subsystems (Kormendy 1993; Fathi & Peletier 2003), sometimes with their own spiral structure, undergoing continuing star formation, and with brightness profiles like those of disks (Kormendy 1977,

1993; Fisher & Drory 2008). These bulges have been coined pseudo-bulges (see Kormendy & Kennicutt 2004, for complete set of pseudo-bulge characteristics) and are thought to originate from secular processes in disks (bars, spiral structure, etc.) (Kormendy & Kennicutt 2004; Athanassoula 2005; Weinzirl et al. 2009). On the other hand, 'classical' de Vaucouleurs-like bulges, are thought to have formed early by hierarchical mergers (Eggen et al. 1962), and acquired their disks later (but see Noguchi 1999; Elmegreen et al. 2008).

For galaxies with classical bulges, the differences between bulge and disk components extend beyond morphology. The stellar populations, mean ages, dynamics, and star formation rates are very different, again suggesting that bulges are very much like ellipticals, which also have old stellar populations, pressure-dominated dynamics, and low star-formation rates. Like ellipticals, bulges have old stellar populations and abundance ratios consistent with an early burst of star formation (Peletier et al. 1999; Moorthy & Holtzman 2006; MacArthur et al. 2008). Additionally, studies have found that classical bulges lie on an extension of the fundamental plane (Falcón-Barroso et al. 2002)(but see Laurikainen et al. 2010), suggesting similar dynamics. The (typically) much higher star formation rates

⋆ E-mail: clackner@astro.princeton.edu

in disks give rise to significant colour differences between bulges and disks. This blue disk/red bulge phenomenon is clearly a major reason for the observed colour bi-modality in galaxies (Driver et al. 2006; Drory & Fisher 2007). However, it is also clear that the real situation is complicated and environment-dependent, with the present-day universe containing both blue elliptical galaxies with ongoing star formation (Schawinski et al. 2009), and galaxies with prominent disks and essentially no star formation activity (Bamford et al. 2009; van den Bergh 2009; Masters et al. 2010).

The existence of the data set from the Sloan Digital Sky Survey (SDSS) makes it possible to investigate the properties of bulges and disks for a very large sample. We present here two-dimensional fits, including the colours for bulge and disks components, for 71,825 main-sample SDSS galaxies with redshifts between 0.003 and 0.05. We attempt from the outset to obtain fits which are astrophysically motivated and which make morphological sense. The population is so complex that this is only partially successful, as we show below. Guided by the division of bulges into classical and pseudo-bulges, we fit either a de Vaucouleurs or exponential bulge and an exponential disk to each galaxy for which a two-component fit makes statistical sense. For the galaxies with signal-to-noise too low to significantly support a two-component fit *and* those for which the bulge plus disk (B+D) fit is physically implausible, despite high S/N, we fit elliptical Sérsic profiles (for which the surface brightness falls as $R^{1/n}$) (Sersic 1968). It is clear from our work that generalizing fits to allow more parameters is not justified, at least for this data set, and studies of bright subsets of our sample suggest that it may not be useful for ground-based images at all.

Both qualitative and quantitative methods for determining galaxy morphology are used. For nearby, well-resolved samples, two dimensional decomposition of galaxy images into bulge and disk components is possible and there are several automated tools available to do such decompositions: `GALFIT` (Peng et al. 2002), `GIM2d` (Simard et al. 2002), `BUDDA` (de Souza et al. 2004; Gadotti 2008), and `GALACTICA` (Benson et al. 2007). These methods have been used to create large samples of bulge-disk decomposed galaxies (Allen et al. 2006; Benson et al. 2007; Gadotti 2009; Simard et al. 2011). With the exception of Simard et al. (2011)(S11), the largest sample consists of 10,000 galaxies from the SDSS early data release (Benson et al. 2007). The sample of S11 includes 1.1 million galaxies from the SDSS Legacy survey using data release 7. This sample includes 96% of the galaxies in the sample presented here; the missing galaxies are brighter than the cutoff in the S11 work. Nonetheless, the numerical methods used in the works are distinct, and the goals of the two studies are not the same. In the future, we plan to use the sample presented in this work to study the properties of disks around classical bulges, and have therefore focused on robust fits to galaxies with statistically significant bulges and disks.

In order to accommodate this large sample, we have written a bulge-disk decomposition pipeline in `IDL` which relies heavily on the SDSS reductions. We use the SDSS sky subtraction, deblending, and point-spread function (PSF) determinations in our fitter. This allows us to quickly fit each galaxy in our sample with 5 different models, using a uniform methodology. In addition to fast fitting algorithms, large samples of bulge-disk decomposition require careful analysis of the systematic errors in estimating bulge and disk components as a function of galaxy size, luminosity, and redshift. At the extremes, for galaxies with sizes comparable to the PSF, a bulge-disk decomposition does not yield meaningful results. Similarly, images of nearby galaxies contain structure which is not accounted for in simple two-component bulge-disk models, yielding poor quality, inaccurate fits. We have examined the systematic errors in our sample by fitting galaxy images while varying the signal-to-noise and resolution of galaxy images, as well as degrading images of nearby galaxies to match those at higher redshift. These tests give an estimate of the systematic and statistical uncertainty in the bulge-disk parameters for the galaxies in our sample.

Due to the size of our sample, we must rely on output of the bulge-disk decomposition to classify the galaxy as an elliptical or disk galaxy, and the bulge as a classical bulge or pseudo-bulge. At high resolution, galaxies are almost always more complex than either of our B+D models. For lower resolution and signal-to-noise images, the two models are often indistinguishable, fitting the galaxy equally well. Therefore, in addition to a goodness of fit, we must on astrophysical constraints in order to quantify the galaxy morphology. Since we expect classical bulges to be elliptical-like and pseudo-bulges to be disk-like, we distinguish between classical and pseudo-bulges based on their colour and ellipticity. Blue, flattened bulges are categorized as pseudo-bulges and assigned an exponential light profile, while red bulges are assigned a de Vaucouleurs profile. We test this division of galaxy type against other measures of galaxy type (e.g. Sérsic index, concentration, fundamental plane relations) and find that the combination of colour information with bulge-disk decomposition yields a reasonable classification of galaxy types. Although we have fit more than 70,000 galaxies with two-component fits, we do not expect these fits to be physically meaningful in all cases. For 50% of our sample we do not attempt to classify bulges as a classical or pseudo, instead, we fit these galaxies with single Sérsic profiles, and set them aside. Some of these galaxies undoubtedly have a bulge and disk, but are not bright enough or sufficiently resolved to support a good B+D fit. However, we find that the majority of galaxies fit with a Sérsic profile are intrinsically faint and blue, and are therefore unlikely to be well-fit by a B+D model.

This paper is divided into sections as follows. In §2 we describe the sample of galaxies. Section 3 describes the fitting procedure and §4 examines the robustness of the fits by examining the impact of changes in signal-to-noise, resolution and redshift. In section §5, we divide our sample into pure disks, ellipticals, disks plus classical bulges and disks plus pseudo-bulges, taking into account inclination corrections (§5.3). Throughout this paper we use the ΛCDM cosmology, $\Omega_m = 0.3$, $H_0 = 70$km s^{-1}, and $\Omega_\lambda = 0.7$.

2   SAMPLE

The sample of galaxies we fit is a low redshift sub-sample of the NYU value-added catalog (VAGC) of the SDSS Data Release 7 (DR7) galaxies (Blanton et al. 2005; Abazajian et al.

2009; Padmanabhan et al. 2008). We have matched the DR7 catalog to objects and images from DR8 (Aihara et al. 2011), and use the later data release images for our analysis. The most important difference between the DR8 and DR7 reductions is the improved sky subtraction around bright, extended objects (Aihara et al. 2011). All the galaxies in our sample are also contained in the SDSS spectroscopic sample. We limit the redshift range of the sample to galaxies with $0.003 < z < 0.05$ and magnitudes $m_r < 17.7$. We further remove all galaxies with poor deblends flagged by the SDSS photometric pipeline. The galaxy fluxes were k-corrected to $z = 0$ using the IDL package kcorrect, v4_2 (Blanton & Roweis 2007). At this point, the sample consists of $87,000$ galaxies.

Because we have chosen to fit simple Sérsic profiles to the galaxies, our models are inaccurate for highly-inclined disk galaxies, where the vertical scale height is significant relative to the minor axis of the projected galaxy. Studies of edge-on disk galaxies have shown that the minimum disk flattening (vertical scale height/disk scale length) is ~ 5 (Kregel et al. 2002), and is independent of galaxy size. However, the *average* disk flattening increases with the maximum rotation velocity of the disk. Flat disk models used to fit highly-inclined galaxies will introduce errors in the surface brightness and the inclination. We have examined the size of these errors as a function of inclination for projected three-dimensional disk galaxy models. We model a disk galaxy as exponential profiles in R and z with a disk flattening of 5, and then fit projections of this model with a flat disk (exponential profile in R) model. When the inclination of the disk is more than $\sim 75°$, (corresponding to an axis ratio of 0.25 for a flat disk), the errors in the measured axis ratio and surface brightness are between 5% and 10%. In order to limit the errors due to poor disk models, we have limited our work to galaxies with axis ratios greater than 0.25, as measured by the SDSS pipeline. This leaves a sample of $79,476$ galaxies.

The images used in the fitter are the SDSS generated atlas images, which contain all the pixels around a source with significant detection. S11 argue that the isophotal cutoff for the atlas images is too bright, leading to significant loss of flux. We can check this by calculating how much of the fitted model flux is outside the atlas image for each galaxy. For single Sérsic profile fits, between eighty and ninety percent of the atlas images contain 90% of the model flux. The uncertainty is due to not knowing how many pixels are excluded from the atlas images because they are part of other objects. The bulge+disk models are missing a comparable amount of light. Unlike the models used in S11, our models are cutoff at large radii, reducing the amount of light missing from the atlas images in our model fits.

The atlas images are deblended and sky subtracted. The value of the sky is the locally measured SDSS sky value, not that of the entire field. The SDSS photometric pipeline, photo, calculates the sky on a grid of 128×128 pixels by taking the clipped median of 256×256 pixels surrounding each grid point. The local sky is obtained by bi-linear interpolation. The new version of photo used in DR8 first subtracts preliminary models (linear combination of de Vaucouleurs and exponential) for the bright galaxies and then takes the median around each grid point (Aihara et al. 2011). This helps eliminate flux from bright extended objects from the

estimate of the sky, a known problem with earlier SDSS reductions (Mandelbaum et al. 2005; Bernardi et al. 2007; Lauer et al. 2007; Guo et al. 2009; Abazajian et al. 2009). The preliminary galaxy models are added back in and refit after the sky subtraction is complete.

3 FITTING

We perform the 2-dimensional fits on the r-band atlas images. Each image is fit five times, using five different profiles, two composite (bulge+disk) profiles and three single component profiles:

   (i) de Vaucouleurs bulge + exponential disk profile
   (ii) exponential bulge + exponential disk profile
   (iii) Sérsic profile
   (iv) exponential disk profile ($n = 1$ Sérsic profile)
   (v) de Vaucouleurs profile ($n = 4$ Sérsic profile)

The functional form of a single Sérsic component is given by the formulae:

$$S = \Sigma_{1/2} \exp\left[-k\left((R/R_{\text{eff}})^{1/n} - 1\right)\right] \tag{1}$$

$$\begin{aligned}R = &\sqrt{\big[((x - x_0)\cos\phi + (y - y_0)\sin\phi)^2} \\ &+ ((y - y_0)\cos\phi - (x - x_0)\sin\phi)^2/q^2\big] \end{aligned} \tag{2}$$

where R_{eff} is the half-light radius of the profile, $\Sigma_{1/2}$ is the surface brightness at R_{eff}, (x_0, y_0) is the central position, ϕ is the rotation angle, q is the axis ratio of the elliptical isophotes, n is the Sérsic index, and k is a normalization factor given by $k = n \times \exp(0.6950 - 0.1789/n)$ (Lima Neto et al. 1999). Therefore, for the single component there are 6(7) free parameters for the de Vaucouleurs and exponential disk profiles (Sérsic profile). For the two component fits, we assume the central position is the same for the bulge and the disk, leaving 10 free parameters for the bulge/disk fits. As with the SDSS de Vaucouleurs and exponential profiles, our model profiles are cut off smoothly at large radii. For exponential (de Vaucouleurs) profiles, the surface brightness is suppressed outside $3(7)R_{\text{eff}}$ and drops to zero outside $4(8)R_{\text{eff}}$.

We have chosen not to allow the Sérsic index of the bulge be a free parameter in the fits. This is done to limit the number of free parameters in the fits. The bulge Sérsic index is highly covariant with the half-light radius of the bulge (Trujillo et al. 2001), and for a typical galaxy in our sample, varying the Sérsic index does not lead to better fits (de Jong 1996, see also). As can be seen in equation 1, the differences between different Sérsic index profiles decreases with increasing Sérsic index. High Sérsic index profiles are sharply peaked and decrease slowly outside R_{eff}. For bulges embedded in disks, the long tail is subsumed in a disk, while the central peak is washed out by the PSF. At a resolution typical for our sample, for a galaxy with $m_r \approx 16.5$, a bulge with $n_b = 4$ and a $B/T \approx 40\%$, the χ^2 value of a fit with an $n_b = 4$ bulge is indistinguishable from one with $3 \lesssim n_b \lesssim 5$. However, for this range of Sérsic index, R_{eff} varies by a factor of 2, which leads to significant variation in the B/T (Graham 2001; Balcells et al. 2003; Graham & Worley 2008). In order to facilitate a comparison with elliptical galaxies, we have chosen to fit classical bulges and ellipticals with a de Vaucouleurs profile. This value for n may be too large for

bulges (and for some ellipticals (Caon et al. 1993)), but it eliminates a parameter which does little to improve the χ^2 values of our fits, and allows us to compare bulge properties to those of ellipticals. Because we anticipate our sample will contain pseudo-bulges and bulges of lower Sérsic index, we have also fit each galaxy with an exponential ($n_b = 1$) bulge + exponential disk. In the latter case, we define the bulge component to be the profile with the smaller R_{eff}. These two bulge Sérsic indices are in broad agreement with the Sérsic indices for pseudo-bulges ($n_b \approx 1.7$) and classical bulges ($n_b \approx 3.5$) found in smaller, high resolution (HST) studies (Fisher & Drory 2008).

The best-fitting parameters for each model are found using the minimization method `mpfit2dfun` in IDL, which performs 2-dimensional Levenberg-Marquadt minimization (Markwardt 2009). The fitter minimizes the weighted sum of the difference between the image and PSF-convolved model. The fitted images are convolved with the locally measured PSF from SDSS. The weight of each pixel is given by its inverse variance. The variance in counts is given by (signal+sky)/gain+dark variance+sky error^2. For sky-dominated images, the variance is constant as a function of galaxy radius. For bright galaxies, the variance is larger, and the weights smaller, at the centres of the galaxies. Although the inverse variance weighting are the optimal weights for a χ^2 fit, they introduce systematics with redshift (and size and brightness): i.e. galaxies at high redshift are fit with nearly constant weights, while bright, nearby galaxies are down-weighted in the centres. For samples covering a larger redshift range, a set of weights which are consistent across the range may be more appropriate. This would entail using less than optimal weights (e.g. using only the sky-noise for the weights) for the highest resolution and brightest galaxies.

The initial parameters for the minimization are taken from the SDSS analysis of the galaxy. The initial fit parameters include the one dimensional de Vaucouleurs or exponential fit scale length, chosen based on `FRAC_DEV`, the relative likelihood of a de Vaucouleurs fit over and exponential fit, `R_(DEV,EXP)`, the angle of rotation of profile, `PHI_(DEV,EXP)`, the axis ratio of either profile, `AB_(DEV,EXP)`. We require that the fitter return positive values (but possibly zero) for the surface brightness for each component. We also place lower limits on R_{eff} (0.1 pixels) and on q (0.05). We allow the minimizer 1000 steps. Fits that do not converge within 1000 steps are considered failed fits. Fits in which either bulge+disk combination fail to converge occur for 2.5% of the sample. Fits in which both B+D models fail occur in less than 20 images in the entire sample. We also exclude galaxies in which the signal-to-noise within R_{eff} is less than 3, for any of the single component fits. This typically excludes diffuse, irregular galaxies for which none of the above models is reasonable. This excludes 3530 galaxies from the sample.

In order to examine the colours of the components of each galaxy, we also fit the g and i-band atlas images of each galaxy. These fits are accomplished by a taking the best-fitting r-band model, and performing a linear least squares for the g and i-band images by scaling the surface brightness, $\Sigma_{1/2}$, for each profile component. Therefore, the profiles fit in each band are the same, only the overall normalizations and the bulge-to-total ratios (B/T) change in the different

bands. This procedure is analogous to the SDSS `modelMag` measurements, which apply the best r-band model (de Vaucouleurs or exponential) to all the filters. These aperture-matched colours are less noisy than those that would be obtained by fitting a B+D model independently for each filter.

We have compared our single component exponential and de Vaucouleurs fits to those from SDSS. Overall, we find good agreement between our fits and those from SDSS when the fit is accurate for a galaxy, i.e. when `FRAC_DEV` is large(small) for de Vaucouleurs(exponential) fits. For the exponential fits, the median difference in r-band magnitude is 0.040 with an inter-quartile range (IQR) of [0.018, 0.072], for all the galaxies. Those with the largest offset are galaxies which have high `FRAC_DEV`, and are poorly fit by an exponential profile. For the de Vaucouleurs model, the median difference in magnitude is -0.159 (IQR=[-0.381, -0.027]). This difference decreases to -0.025 (IQR=[-0.065,0.017]), if we restrict the comparison to galaxies with `FRAC_DEV`> 0.5. This suggests that our fully 2-dimensional models fail differently than the SDSS single component models. The cause of this is probably related to how the image is cut off at large radii; de Vaucouleurs models are much more sensitive to extended flux than exponential models, making the differences larger. For the exponential fits, the half-light radii measured agree to within $\lesssim 5\%$ for all fits and to $\lesssim 3\%$ for fits with `FRAC_DEV`< 0.5. For the de Vaucouleurs R_{eff}, the difference in R_{eff} is larger, with a median difference between the SDSS R_{eff} and our R_{eff} of -9%, for galaxies with `FRAC_DEV`> 0.5. This difference is the main reason our magnitudes are systematically brighter than the SDSS de Vaucouleurs magnitudes. Furthermore, the fractional difference in scale length increases with increasing R_{eff}. The difference in scale length has several causes. First, the SDSS fits use a maximum allowed scale length of 80 pixels while we allow R_{eff} to take any value larger than 0.01 pixels. Second, the de Vaucouleurs profiles in SDSS are softened within $R_{\mathrm{eff}}/50$ in order to allow for a large dynamic range in surface brightness. We do not use this softening, which leads to slightly larger values for R_{eff}. The galaxies with the largest values for R_{eff} are almost always better fit by a two-component or Sérsic model fit, so the large differences between our fits and those in SDSS occur for galaxies for which the de Vaucouleurs model is inaccurate, and therefore are not a large concern.

We also compare our single component Sérsic fits to those found by Blanton et al. (2005), which use the azimuthally-averaged radial profiles from the SDSS `photo` pipeline. We find systematically higher Sérsic indices for $n \gtrsim 3$. This difference arises from the following sources. We allow Sérsic indices to vary between 0.1 and 9 while the Blanton et al. (2005) Sérsic indices do not exceed 6. Additionally, Blanton et al. (2005) find that their high Sérsic indices are underestimated by ~ 0.5 at $n = 4$, and claim this is due to uncertainty in the sky. Our measurements are done on DR8 images which have improved sky estimates. Finally, the details in the cutoff radius are not the same, which will effect the high Sérsic index galaxies more than the low Sérsic index galaxies. The mismatch between our measured Sérsic indices and those from Blanton et al. (2005) is similar to the mismatch found by S11.
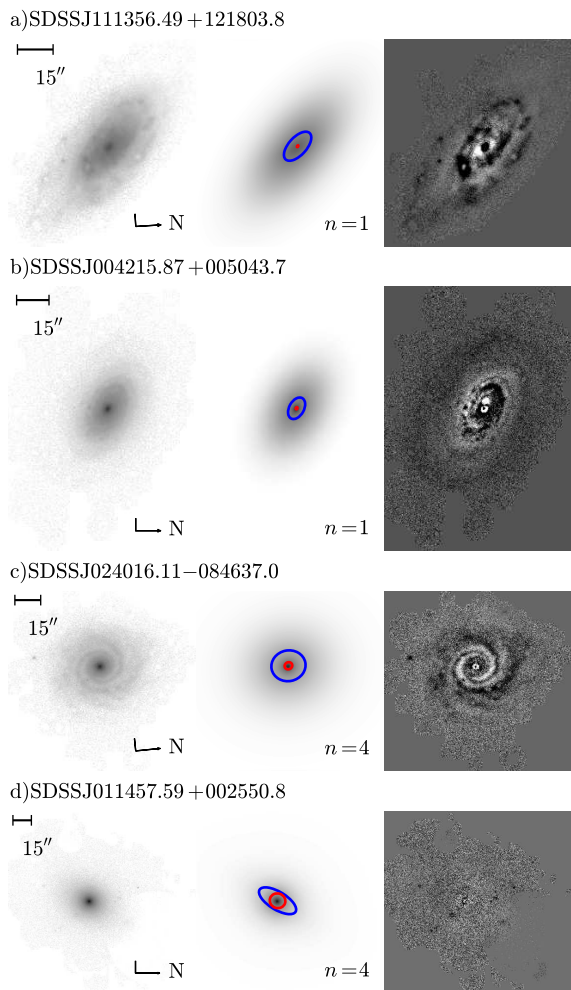
a)SDSSJ111356.49+121803.8

15″

N $n = 1$

b)SDSSJ004215.87+005043.7

15″

N $n = 1$

c)SDSSJ024016.11−084637.0

15″

N $n = 4$

d)SDSSJ011457.59+002550.8

15″

N $n = 4$

Figure 1. Images of fitted galaxies. The first column is the SDSS $r-$band image, the center is the model fit with an $n = (1, 4)$ bulge, and the final column is the residual. The blue ellipse contains 1/2 the light from the disk, while the red ellipse contains half the light from the bulge.

3.1 Examples of fits

Figure 1 shows B+D fits for four bright, well-fit galaxies, in order of increasing B/T. The top two galaxies are shown with an $n_b = 1$ bulge fit, while the bottom two are shown with an $n_b = 4$ fit. The model fit is chosen based on the relative χ^2 values of the different B+D fits. The residuals are shown in the far right column. The 1−dimensional profiles for these galaxies are shown in Figure 2.

The last panel in Figure 1 is an elliptical galaxy; however the fit includes a large, low surface brightness exponential component along with the $n = 4$ component. The χ^2 value of this fit is statistically significantly better than the fit to a pure de Vaucouleurs profile. The B/T ratio of this galaxy is 0.86. The exponential component has a central surface brightness > 27 mag arcsec^{-1}, and a signal-to-noise of 1.7 within $R_{\rm eff}$. If the bulge were subtracted from the image, the disk alone would be undetectable. Because we ignore galaxies for which S/N for a single component fit is less than 3, we have also removed individual compo-

nents from our B+D fits which have S/N< 3. Therefore, SDSSJ011457.59+002660.8 is best fit by a single de Vaucouleurs profile. Additionally, the $g − r$ and $g − i$ colours of exponential and de Vaucouleurs components for this galaxy are the same to within uncertainty. This suggests the exponential component is most likely not a disk, but simply a reflection of the fact that the galaxy is not a perfect de Vaucouleurs profile. The best-fitting Sérsic profile for this galaxy has $n = 4.4$, which helps account for the exponential profile at large radii. These so-called fake disks are a known problem for automated bulge-disk decompositions (Allen et al. 2006; Cameron et al. 2009). One solution is to set a maximum B/T for two component fits and fit everything above the cutoff with a single Sérsic model (Allen et al. 2006). Additionally, these exponential components are characterized by having similar ellipticity to their bulge as well as similar colours, and can be successfully removed based on a combination of these three characteristics. We discuss choosing between the five different model fits in §5.1. Tables containing all the models fit to each galaxy as well as our best-fitting model for each galaxy are available for download.[1]

4 QUALITY OF FITS

In order to assess the quality of the fits, we have created two sub-samples. The first, Sample A, is a hand-selected sample of 30 bright ($M_r > 13.5$) galaxies which span a range of B/T and q values. These galaxies are well fit by either B+D model, but many of them have extra structure, such as spiral arms. We use this sample to test the effects of degrading signal-to-noise and the resolution in our images. The second sub-sample, Sample B, is a sample of 190 galaxies which span the magnitude and redshift range of our sample. The selection of this sample is random and not based on the quality of the fits, but galaxies for which either B+D model failed to converge have been removed.

4.1 Colours

One way to test the robustness of our B+D decompositions is to perform the full 2-dimensional B+D decomposition in the g and i bands as well as the r-band. We have done this for Sample B. This test allows use to estimate the errors of the colours of the bulge and disk components as measured from the linearly scaled g and i band fits. From the reduced χ^2 values, a probability value for accepting/rejecting the model can be calculated from

$$p = \int_0^{\chi^2} P_\chi(\nu, \chi) \qquad , \qquad (3)$$

where ν is the number of degrees of freedom and P_χ is the χ^2-distribution for ν degrees of freedom. Unlike the reduced χ^2 values, the probabilities can be directly compared between the linearly scaled fits and the full model fits. While the average difference between p-values for the full model fit and the linearly scaled fits is 5% and 4% in the g and i-bands, respectively, the median difference in p-values is 0.

---

[1] See http://www.astro.princeton.edu/∼clackner/home/research for the complete data tables.
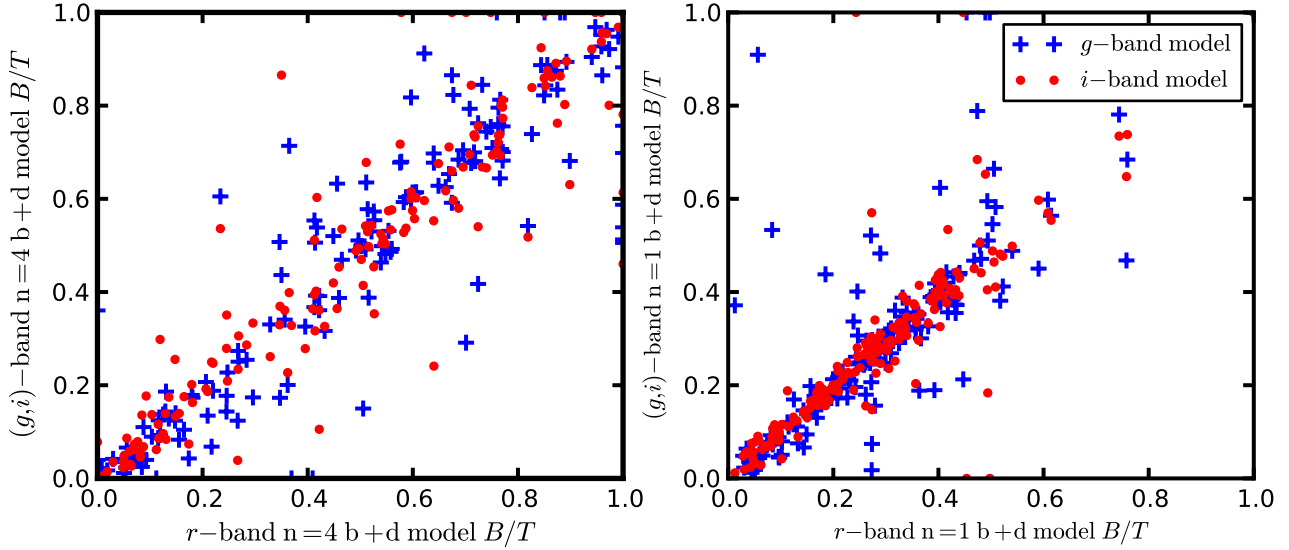
Figure 3. Comparison of the B/T for an $n_b = 4$ B+D model (left) and an $n_b = 1$ B+D model (right) in the $r-$band for galaxies fit in the $g,r,$and i bands. The $x-$axis is the B/T of the model fit in r. The blue crosses show the B/T in r measured by scaling the model fit to the g-band. The red points are the same for the i-band.

In addition to comparing the quality of the fits in the different bands, we also compare the actual parameters obtained in g, r, and i. We find no systematic trends in B/T with either magnitude or B/T, although there is significant scatter. Figure 3 compares the B/T in r measured using the models fit in g, r, and i. The B/T values for g and i-band models are obtained by linearly scaling those models to fit the r-band image. Since we are comparing B/T in one band, we expect the differences to be consistent with zero. Indeed, for the $n_b = 4$ fits, the median values of $(B/T_r - B/T_{g,i})/B/T_r$, where the subscript refers to the model, are 0.02 (IQR=[−0.04, 0.11]) and 0.01 (IQR=[−0.06, 0.10]). For the $n_b = 1$ B+D fits, the same quantities are 0.02 (IQR=[−0.04, 0.08]) and 0.05 (IQR=[0.02,0.09]). All but the last value is consistent with zero. For the exponential bulge fits, the large scatter at higher B/T is due to difficulty in separating the bulge from the disk when they have the same functional form. The uncertainty in the B/T measured in the different bands is directly related to the uncertainty in the colours of the different components. A difference in B/T of 7% corresponds to a difference in bulge colour of -0.07. If instead of comparing B/T measured in one band, we compare the B/T measured in different bands, we expect the differences to be consistent with the colour differences between bulges and disks. Since bulges are redder than disks, B/T should be largest in the redder filters. Looking at galaxies which are categorized as bulge+disk galaxies (see §5.1), bulges are typically 0.11 magnitudes redder than the total galaxy in $g - r$. Similarly, the median value of $(B/T_g - B/T_r)/B/T_r = 0.13$, where the subscript refers to the filter B/T is measured in. This agrees well with difference between bulge and total galaxy colours.

Comparisons of the scale lengths measured in the different filters is shown in Figure 4. The fit parameter with the largest scatter is the $n_b = 4$ bulge $R_{\rm eff}$. For galaxies with r-band measured $B/T > 0.1$, the scatter in the de Vaucouleurs bulge $R_{\rm eff}$ is $\sim 20\%$. The scatter in the exponential bulge

$R_{\rm eff}$ is $\sim 15\%$. The scatter in the disk $R_{\rm eff}$ in all three filters is $\lesssim 10\%$. The large scatter in the de Vaucouleurs scale length is related to the steepness of the $n = 4$ Sérsic profile compared to an exponential profile. Small changes in the measured central flux yield large changes in the measured $R_{\rm eff}$. Figure 4 shows the relative difference between the r-band measured $R_{\rm eff}$ to those measured in the g and i images. There is no systematic offset in the values, although the scatter in the bulge (disk) scale length measurements grows with increasing (decreasing) B/T. Although the scatter in the $R_{\rm eff}$ is consistent with no systematic difference in $R_{\rm eff}$, the g-band models tend to have slightly larger scale lengths than those in r and i. This is consistent with the observation that galaxies are bluer on the outskirts (Franx et al. 1989), thus the scale lengths in the blue bands should be larger. The same phenomenon can be observed in the single Sérsic component fits. In this case, the scale lengths measured in the different bands are consistent to within 5%, but the Sérsic indices measured in the bluer bands are consistently larger, which increases the flux at larger radii, as expected. Offsets of a few percent in the scale lengths are in agreement with the results of the separate band-pass fits in S11.

4.2 Signal-to-Noise and Resolution

In this section, we explore the effects of degrading the signal-to-noise (S/N) and resolution of our galaxy sample images. Although, our sample spans a small range in redshift, it is important to understand the systematics introduced by changing the resolution and the S/N, and the limits on the resolution and S/N at which our fits are no longer reliable. In order to examine these effects, we have performed several tests. First, we have taken mock images of single Sérsic component galaxies at various S/Ns and resolutions. Fits of these mock images are compared to the input model. Although mock galaxies offer some insight, we also take the 39 high resolution, high S/N galaxies in Sample A and create
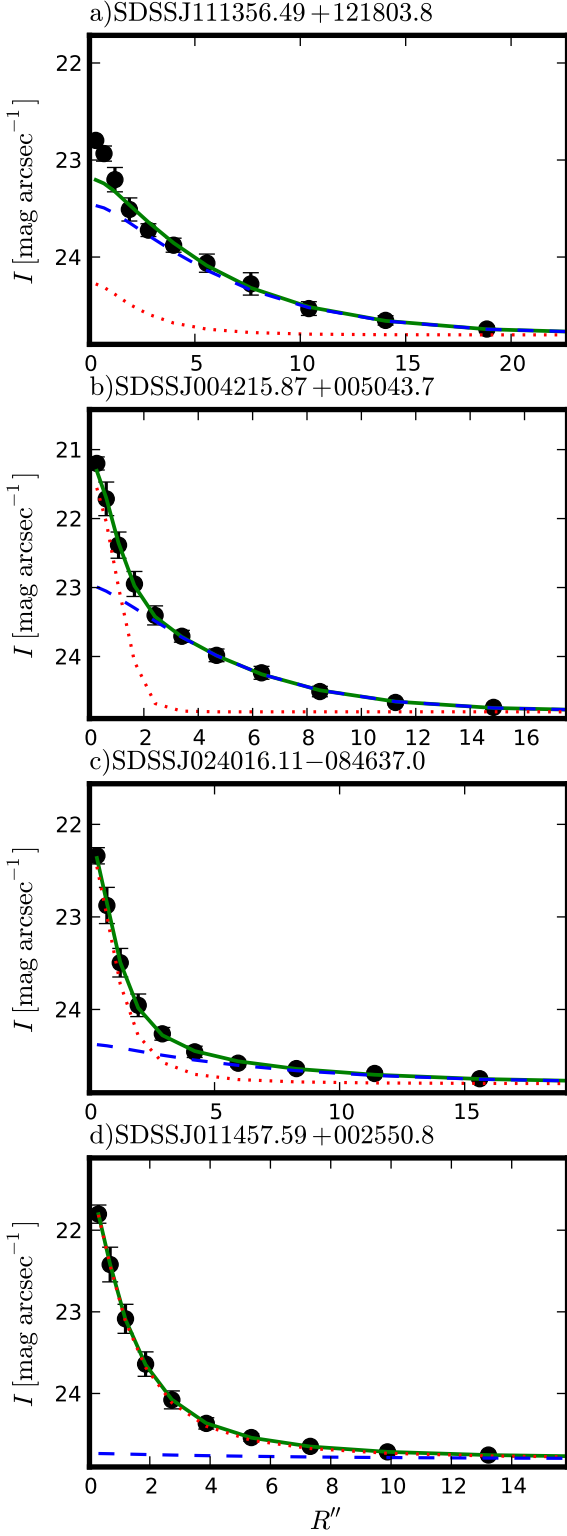
Figure 2. The one-dimensional profiles of the galaxies in Figure 1. The axis along which the profile is taken is the semimajor axis of the bulge or disk, depending on which has a larger $R_{\rm eff}$. The surface brightness is the mean surface brightness in elliptical annuli with axis ratios and position angles taken from the bulge or disk. The points are the surface brightness of the image with errorbars denoting the standard deviation of the flux in an annulus. The green solid line is the model flux. The blue dashed line is the disk flux and the red dotted line is the bulge flux.
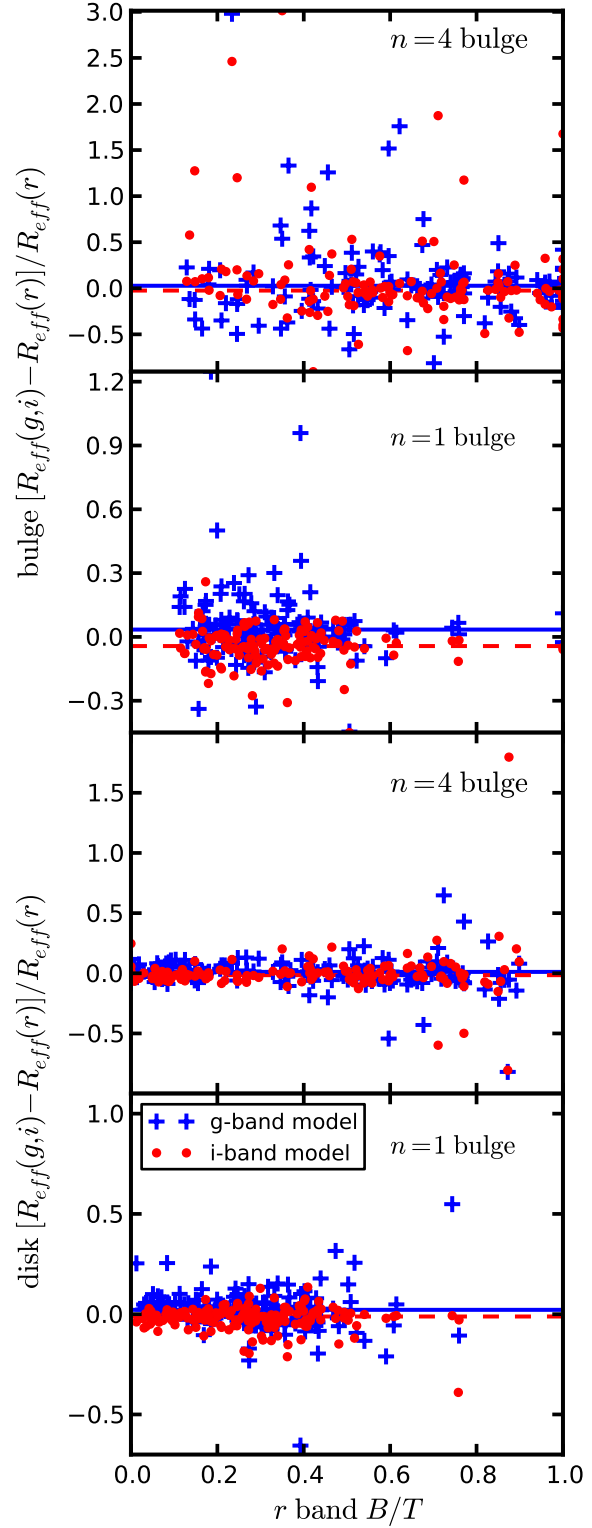
Figure 4. Comparison of the scale lengths fit in g and i to those found using the r-band images. The top two figures show the relative difference in bulge $R_{\rm eff}$ for an $n_b = 4$ B+D (top) and an $n_b = 1$ B+D (second). Galaxies with $B/T < 0.1$ in any band are not shown. The bottom two figures show the same for the the disk $R_{\rm eff}$, with galaxies with $B/T > 0.9$ in any band removed. The blue solid (red dashed) lines show the median difference between the g (i) and r band fits.

new images of these galaxies both at lower resolution and lower S/N. We then run the fitter on these degraded images and compare the results to the original fit of the galaxy. Finally, we examine the combined effect of changing resolution and S/N by taking the images in Sample A and degrading the S/N and resolution simultaneously to create images of the same galaxies as they would look at higher redshift. We define the signal-to-noise ratio for each pixel as the object flux divided by the noise, the square root of the total flux (object *plus* sky) divided by the gain.

The mock images used are single Sérsic component galaxies with R_{eff} fixed at 10.6, 15.2, 21.0, or 36.2 pixels and a Sérsic index of 1, 2, 3, or 4. The surface brightness at R_{eff} is the same for all the galaxies, and the total magnitudes of the galaxies vary from $12.7 > M > 13.9$, similar to the Sample A galaxies. The mock images are convolved with a Gaussian PSF with FWHM=2.9 pixels, the median from Sample A. We add noise to the images assuming a sky background of 115 counts/pixel, the median sky level from Sample A. These are the initial mock images. We then create two sets of degraded mock images, one in which the PSF FWHM is increased, degrading the resolution, and one in which the sky background is increased, degrading the signal-to-noise. For the decreased resolution images, we convolve the mock galaxies with a PSF with FWHM $2.9 \times (1.5, 2, 4, 5, 6, 7, \text{and} 10)$. We do not change the sky background, the galaxy properties, or the pixel size. For the decreased S/N images, we hold everything constant except the sky background, which is increased by factors of 1.5^2, $2.^2$, 4^2, 5^2, 6^2, 7^2, and 10^2. For sky-noise dominated images, this decreases the S/N by the square root of the above factors. We create each mock image multiple times with different noise realizations in order to estimate the scatter in the fit parameters. Since these mock images are exact Sérsic profiles, a single component Sérsic profile fits well. However, as images are degraded, the errors in the Sérsic index increases, to $\sim$ 5-10% at a factor of 10 degradation.

The exponential and de Vaucouleurs fits to mock galaxies with $n \neq 1$ or $n \neq 4$ show interesting systematic changes in R_{eff}. Since we have chosen to fix the Sérsic index of the bulge, we perform these tests to examine the systematics of fitting a fixed n profile to an arbitrary Sérsic profile. If the Sérsic index of the model is too low, the fitted value for R_{eff} systematically increases if the resolution is degraded and decreases if the S/N is degraded. The opposite occurs if the Sérsic index of the model is too high. The magnitude of these two effects is $\sim$ 10-15%, and roughly equal. For a galaxy 'moved' to a higher redshift, the effects should approximately cancel. These trends are clearly present in the real galaxies of Sample A as well and are shown in Figure 5, which shows the change in R_{eff} as a function of original Sérsic index. The cause of these trends is explained by the shape of Sérsic profile. For high Sérsic index, the profile has a sharp peak at $R = 0$ and falls slowly at large radius. Therefore, when fitting a profile with a too low Sérsic index to a mock image, the model underestimates the flux in the center and overestimates the flux in the outskirts. The opposite is true for a model with a Sérsic index that is too large. As the resolution is decreased, the peak at $R = 0$ is smoothed out, and χ^2 is dominated by the flux at large radius. This will increase(decrease) R_{eff} of a model with a Sérsic index smaller(larger) than the actual galaxy. As the
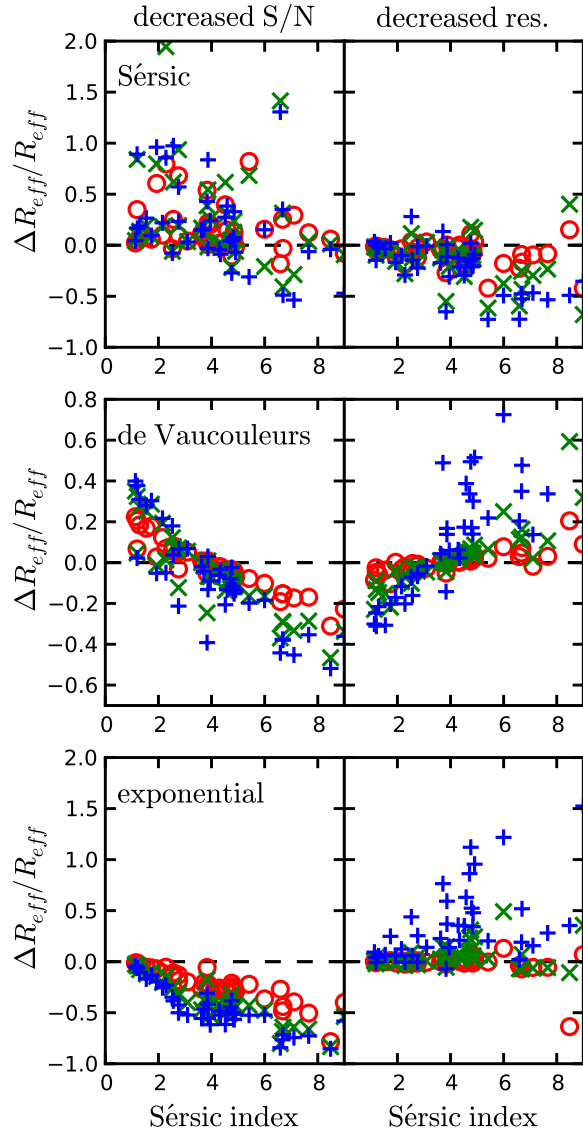

Figure 5. Fractional change in measured R_{eff} as a function of Sérsic index for Sample A galaxies. The red circles show an increase in the sky noise by a factor of 2 (left), and increase the PSF width by a factor of 2 (right). The green ×s and the blue crosses show increases in the sky noise and the PSF width by a factor of 4 and 10, respectively. These changes are equivalent to the changes that would occur in resolution and S/N if the galaxy were moved farther away by a factors of 2, 4, and 10 (in a flat cosmology).

S/N is decreased, the flux at large radius becomes statistically undetectable, and therefore the residuals in center of the galaxy dominate in the χ^2, which lead to smaller(larger) R_{eff} in the exponential(de Vaucouleurs) fits, respectively.

For the real galaxies in Sample A, we have fit images with the same decreases in S/N and resolution as those listed above for the mock galaxy images. These factors are a reasonable choice because they span the properties of our entire sample. A galaxy with the median model magnitude in Sample A ($m_r = 13.25$) would have to be moved $\sim$ 8 times farther away to be below the SDSS spectroscopic sample magnitude limit. The ratio between the median size (as mea-
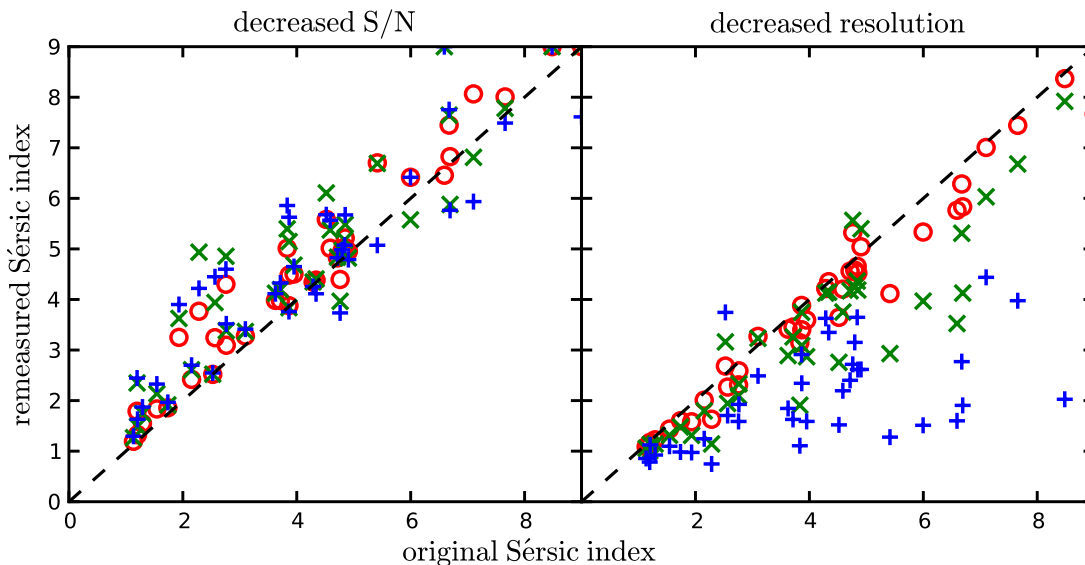
Figure 6. Comparison of the Sérsic index fit to Sample A galaxies while decreasing S/N (left) and resolution (right). The symbols are the same as in Figure 5.

sured by the SDSS value for the radius containing 90% of the Petrosian flux) of galaxies in Sample A and the faintest ($m_r < 17.5$) galaxies in the sample is ~ 4, well within the range of our degraded Sample A images. Because we do not have the underlying galaxy model for the real images, we change the resolution by convolving with a Gaussian PSF with a width $\sigma = \sqrt{(f^2 - 1)}\sigma_{\text{SDSS}}$, where f is the factor of the resolution decrease and σ_{SDSS} is the FWHM of the Gaussian fit to the SDSS PSF. After convolving with the additional PSF, we add back the noise that has been smoothed away, in order to keep the S/N of the image the same as the original. This procedure ignores the fact that the smoothed noise is correlated. To lower the S/N, we add sky noise as if the mean sky background changed by a factor of f^2, which decreases the S/N in the sky-dominated parts of the image by a factor of f. This procedure is no different than that for the mock galaxy images.

For the single-component fits, the results of decreasing the resolution and S/N can be seen in Figures 5, 6, and 7. As with the mock galaxy images, the R_{eff} is sensitive to the Sérsic index of the galaxy. Figure 5 shows the fractional change in R_{eff} as a function of Sérsic index fitted at high resolution. The different markers indicate different fractional changes in S/N and resolution. The top row in this figure shows the change in R_{eff} of a fit with a free Sérsic index. Decreases in resolution(S/N) lead to decreases(increases) in R_{eff}. Since the Sérsic index and R_{eff} are covariant, this trend is also apparent in Figure 6, which plots the Sérsic index from the degraded images against the originally measured Sérsic index. Unsurprisingly, the trend in resolution is most pronounced for high Sérsic index galaxies, which are the most peaked at $R = 0$. The magnitudes of the models fit at decreased resolution and S/N are covariant with R_{eff}, although the change in magnitude is not large, with the magnitude difference between -0.06 and 0.08, while the R_{eff} changes by as much as a factor of 2. The difference in magnitude between the exponential and de Vaucouleurs model fits to the same galaxy can be as large as 0.8. Therefore,

the measured magnitude is reasonably robust to changes in resolution and S/N.

The results of changing S/N and resolution for single component model fits can be understood from the properties of Sérsic profiles and the effects lowering the S/N and resolution have on the outskirts and centers of the profiles as explained above. However, the effects of resolution and S/N on B+D fits are more complicated, and the systematics are less clear. Figure 8 shows the change in model magnitudes as a function of B/T for the two B+D models. While the $n_b = 4$ B+D model fits show no trend, the scatter is larger than the scatter in magnitude for the single component fits. The $n_b = 1$ B+D fits show the same trends in the magnitude with B/T that the single component exponential fits show in magnitude as a function of Sérsic index. This is unsurprising, as the $n_b = 1$ B+D fits are a linear combination of 2 exponential fits and should be subject to some of the same systematics. Figure 9 shows no clear trends in B/T with decreased resolution or S/N. The median fractional errors in B/T for the $n_b = 4$ B+D fit as the S/N decreases by factors of 2, 4, and 10 are 0.01, 0.03, and 0.05. For a decrease in resolution by the same factors, the errors are -0.01, -0.02, and -0.11. For the $n_b = 1$ B+D fits, the equivalent errors are -0.05, -0.10, and -0.13 for decreasing S/N, and 0.06, 0.13, and 0.50 for decreasing resolution. The large change in B/T for the $n_b = 1$ B+D fits can be seen in the lower right panel of Figure 9. As the resolution decreases, the fitter has more difficulty distinguishing between the two $n = 1$ Sérsic profiles in the exponential bulge model. Therefore, small values of B/T will be scattered upwards as more disk light is confused with the bulge.

For the $n_b = 1$ B+D, the bulge and disk scale lengths behave the same way the single exponential scale lengths does; as the resolution(increases) decreases R_{eff} increases(decreases). The effect is especially dramatic for the $n_b = 1$ bulge; the median error in the bulge R_{eff} for a change in resolution by a factor of 10 is 170%. This is shown in Figure 10 for the bulge and Figure 11 for the disk. For the
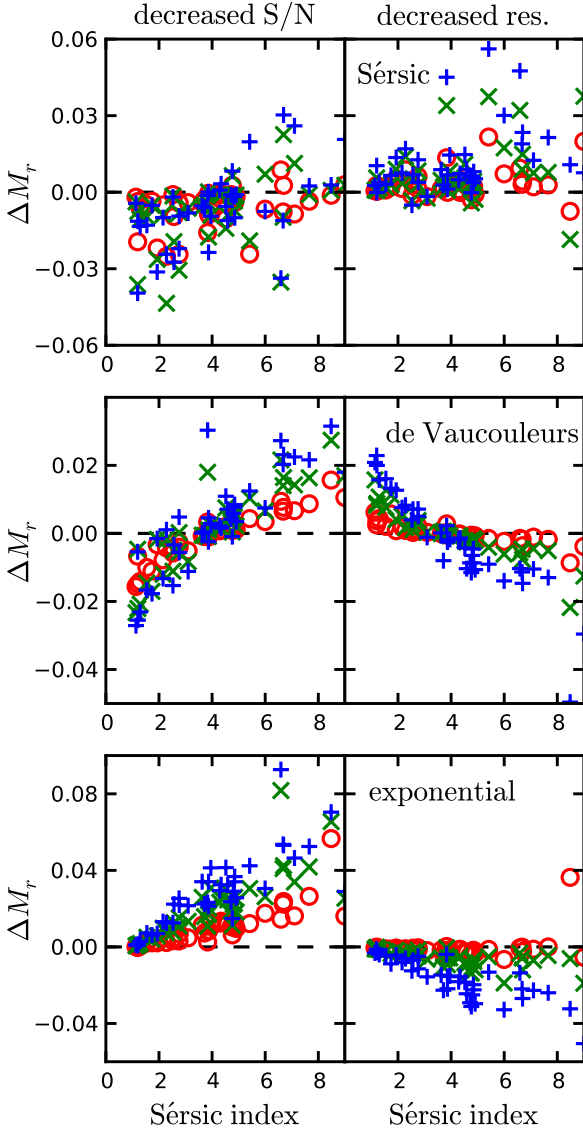
Figure 7. Change in measured r-band magnitude with decreased S/N(left) and resolution(right) as a function of Sérsic index for Sample A galaxy images. The symbols are as in Figure 5.
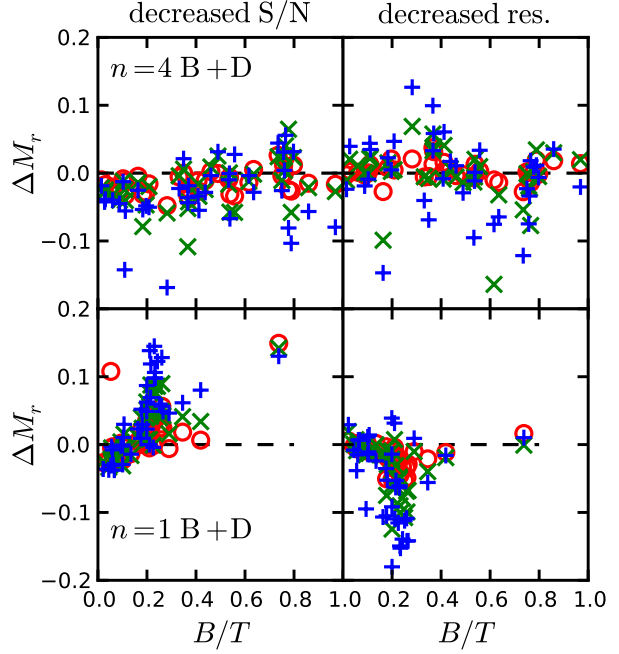

Figure 8. Change in measured r-band magnitude for B+D models with decreased S/N(left) and resolution(right) as a function of B/T for Sample A galaxy images. The symbols are as in Figure 5.

by $\pm 40\%$. Points in the figures show the median and interquartile range of multiple fits to the same galaxy, with different noise realizations.

4.3 Redshift

In addition to varying the S/N and resolution separately for the galaxies in Sample A, we also modify the galaxy images to create mock images of the same galaxy at higher redshifts. These redshifted images involve both a decrease in resolution and S/N as well as a k-correction. For the redshifted galaxies, we rebin the images to decrease the resolution, thus keeping the PSF the same size in pixels. In §4.2, we simply convolved the image with a larger PSF. We do not k-correct the bulge and the disk separately, but instead use a single k-correction for the entire galaxy from `kcorrect` (Blanton & Roweis 2007). In order to compare the results of changing redshift to the results of changing S/N and resolution, we move the galaxies in redshift such that their angular size decreases by factors of 1.25, 1.5, 2, 4, 5, 7, and 10. Figure 16 shows the change in magnitude as the images are moved to higher redshift. This figure is analogous to Figure 7 for decreased resolution and S/N. With the exception of a few galaxies, the errors in magnitude for the exponential and Sérsic fits are small. The trend in de Vaucouleurs fits has the same sign at low n as the trend in magnitude with decreasing resolution, making the high redshift galaxies slightly too bright. This is mainly due to an overestimate of flux in the central regions by a de Vaucouleurs profile.

Figure 17 shows the trend in measured Sérsic index with increasing redshift. The error in Sérsic index for a factor of 2 increase in distance is small. However, the general trend is for the Sérsic index to decrease with redshift, which also
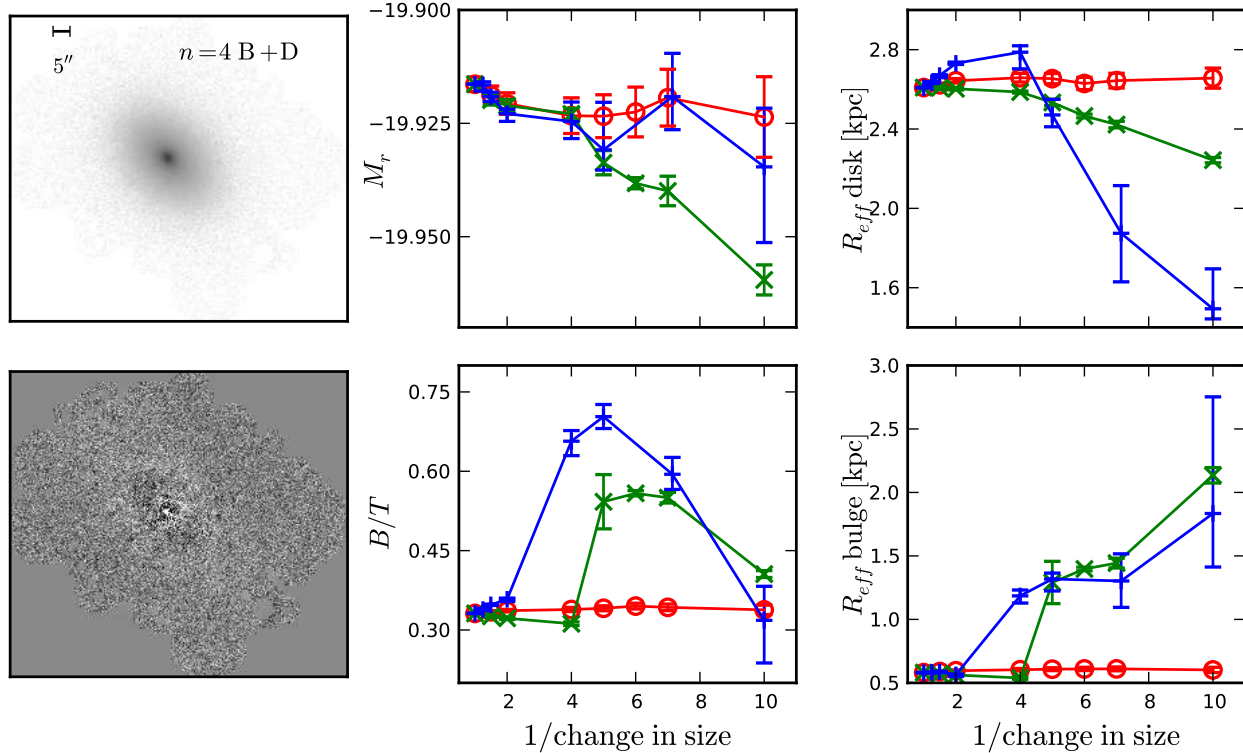
$n_b = 4$ B+D fits, the bulge and disk scale lengths change with the opposite sign for decreasing resolution, but the additional noise mainly adds scatter. The rms error in the $n_b = 4$ B+D model bulge(disk) R_{eff} is 16%(7%), when the S/N is decreased by a factor of 2.

Figures 12, 13, 14, and 15 show examples of 4 different galaxies and their fit parameters at decreased S/N and resolution, and increased redshift (see §4.3). Although these galaxies follow the general trends explained above, these trends are not robust. Figures 14 and 15 show two edge-on disk galaxies, with similar B/T, however, the trends in B/T move in opposite directions for decreasing S/N and resolution. These figures demonstrate the difficulty in establishing the systematic behavior of the model parameters with changes in resolution, S/N, or redshift. They also show which parameters are the most reliable; the total magnitudes never vary more than 0.2 mags, while the B/T changes

Figure 12. Change in model parameters for the galaxy pictured. The model used is named in the first panel. The lower left panel shows the residuals (black is high and positive). The blue lines with crosses show the changes with increasing redshift, i.e. $x = 2$ corresponds to an increase in redshift such that the angular size decreases by a factor of 2. The green $\times$s show the changes with decreasing resolution, i.e. at $x = 2$ the image is convolved with a PSF twice as large as the original. The red circles show the changes with decreasing S/N, i.e. at $x = 2$, the noise is increased by a factor of 2 as it would be if the galaxy were moved twice as far away.

occurs as the resolution decreases, suggesting that for SDSS, the measurements of small galaxies are primarily resolution limited. Figures 12 through 15 also show the changes in the measured parameters with increasing redshift (blue lines). As with the single-component fits, the redshifted images are more similar to the low resolution images than the low S/N images described in the previous section. However, the scatter is typically larger for the redshifted galaxies. For the $n_b = 4$ B+D model, the median fractional error in B/T is -0.06, 0.05, and 0.18 for decreases in angular size by factors of 2, 4, and 10. The equivalent errors in the $n_b = 1$ B+D models are 0.12, 0.35, and 1.26 (See Figure 18). These values are all larger than those found by changing the resolution and S/N separately. The reason for this is two-fold: the redshifted galaxy images are rebinned such that the size in pixels becomes smaller, making the scale lengths more difficult to measure, and the redshifted galaxies are made dimmer and k-corrected which decreases the S/N more than simply increasing the sky counts, especially in the brightest parts of the galaxy. Although the B/T measurements at increasing redshift are dominated by scatter, the general trend in an increase of B/T with increasing redshift, in agreement with other studies (Gadotti 2008; Simmons & Urry 2008).

4.4 Limits on fits and systematics

The tests on mock and real galaxy images above suggest that limits can be placed on the resolution and S/N of images it is possible to fit. One way to quantify the limits on the fits is to examine the relative errors in the fits parameters ($R_{\rm eff}$, Sérsic index, etc.), to the relative errors in the flux. For the bright, well-resolved galaxies in Sample A, the median relative errors of $R_{\rm eff}$ and n for single-component Sérsic fits are $\sigma_{R_{\rm eff}}/R_{\rm eff}/\sigma_{\rm mag} \approx 1.5$, and $\sigma_n/n/\sigma_{\rm mag} \approx 2$. This is in rough agreement with the ratio of uncertainties from linear calculations (Gunn, priv. comm.). As the resolution decreases, the uncertainty ratios increase sharply. Thus the determination of $R_{\rm eff}$ is increasingly uncertain (compared to the flux determination) at low resolution. The same trend holds for the Sérsic index measurement error for a single component Sérsic fit. In this case, the relative error of the Sérsic index increases a factor of 6 over the flux error as the resolution decreases by a factor 10. In order to keep the relative error in $R_{\rm eff}$ and n comparable to the relative error in flux (which is set by the S/N), $R_{\rm eff}$ should be $\gtrsim 0.5 \times$ FWHM. It is also important to note that the Sérsic index, $R_{\rm eff}$, and the total luminosity are highly covariant; small errors in any one of these quantities correlates with errors in the other two. For example, under-estimating the Sérsic index due to low S/N will lead to underestimated values for $R_{\rm eff}$ and the total luminosity. The two-component fits are, of course, more complicated with even more covariances, and the sys-
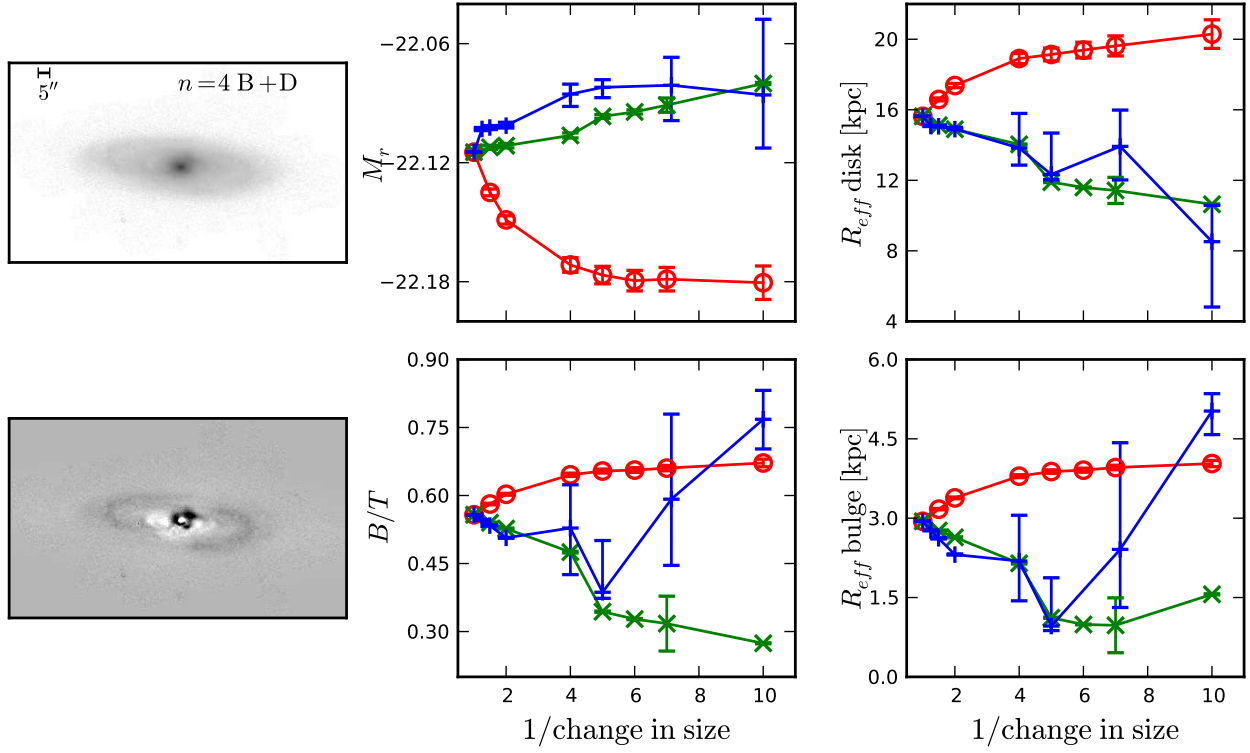
Figure 13. See Figure 12.
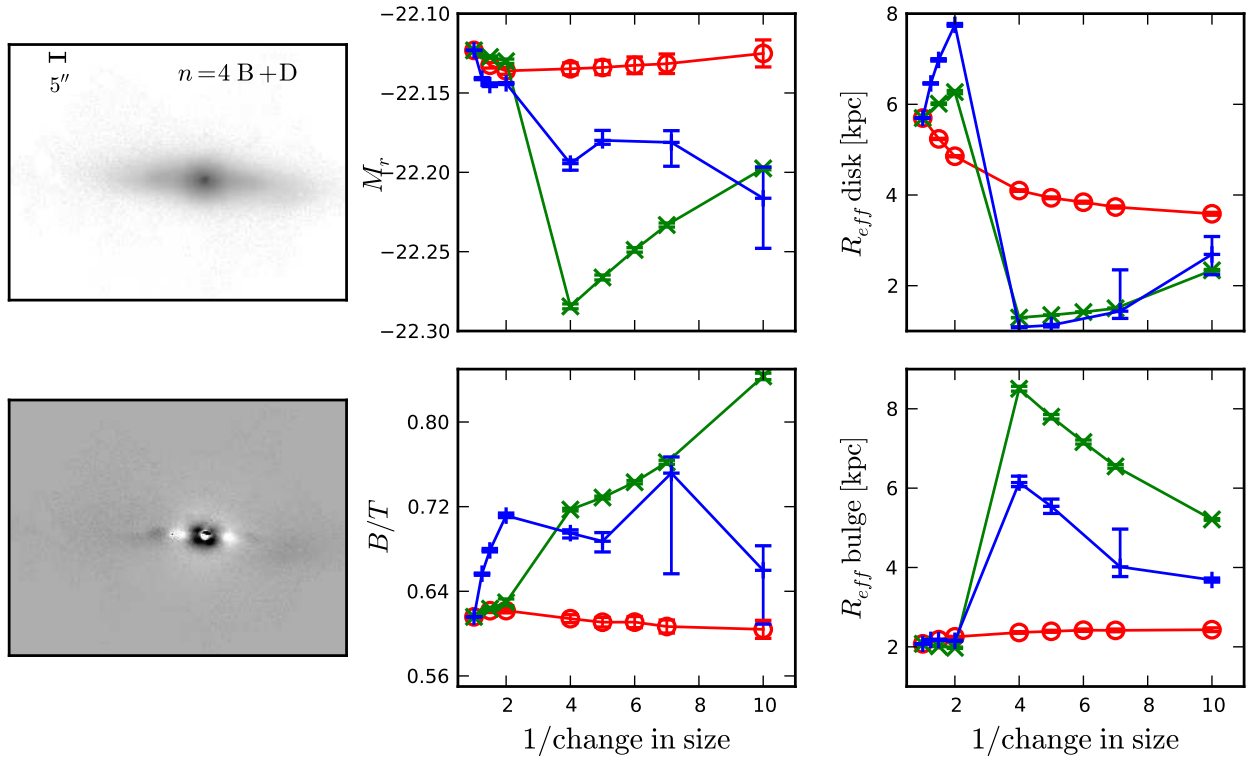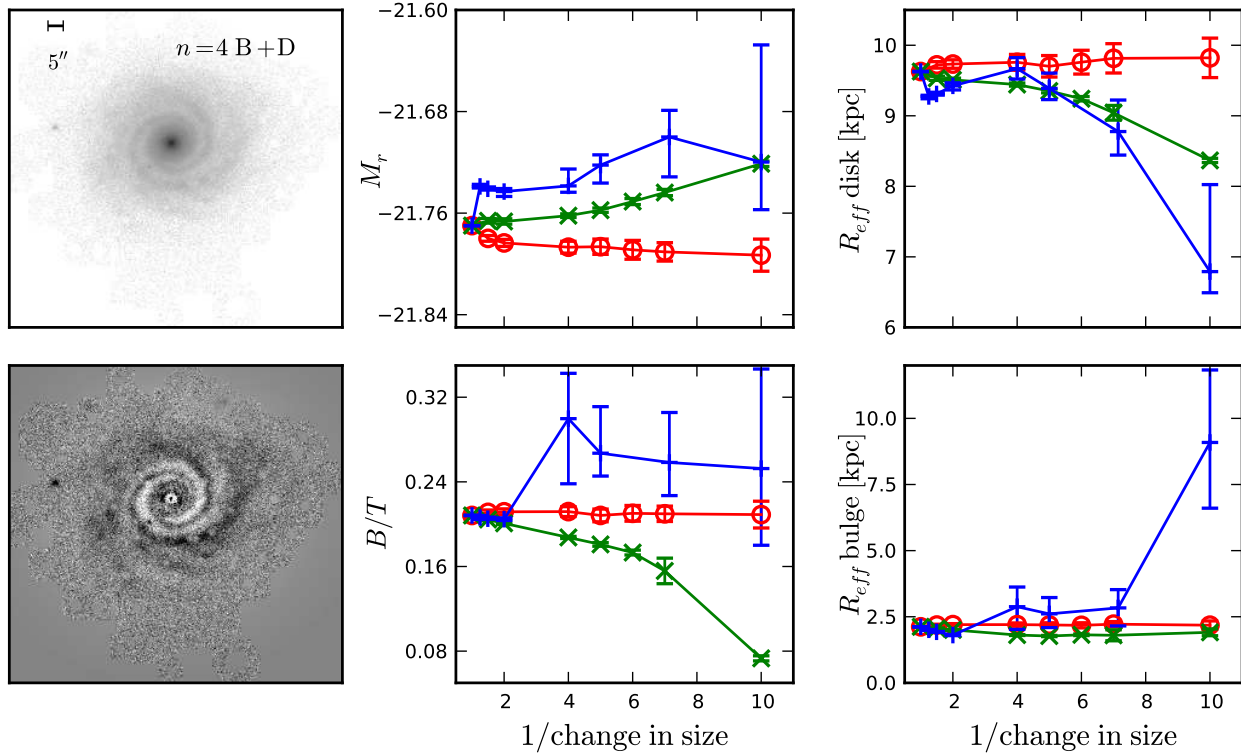

Figure 14. See Figure 12.

Figure 15. See Figure 12.

tematics with S/N and resolution are not easily discerned, but the limit on $R_{\rm eff}$ of 0.5 FHWM is a reasonable choice for bulges and disks in the 2-component fits. In our sample of B+D modeled galaxies, 95% of bulges(disks) have $R_{\rm eff} > 0.4(2.0) \times$ FWHM, suggesting that most bulges are well enough resolved to be adequately measured.

5 ANALYSIS OF FITS

Although we have models for all the galaxies in the sample, for the further analysis we will remove galaxies for which either B+D model fails. This occurs in 5% of the sample which leaves $75,357$ galaxies. We also remove all galaxies for which any of single component fits have a $S/N < 3$ within $R_{\rm eff}$, leaving $71,825$ galaxies. All of the removed galaxies are, on average, intrinsically fainter ($\Delta M_r \approx 0.84$) and bluer ($\Delta(g-r) \approx -0.1$) than the remaining sample. This suggests that these galaxies are often small, irregular star-forming galaxies for which our models are poor. Each of these galaxies is fit by five different models, and, in order to study bulges, we will need a metric for choosing which model to use for each galaxy. Although our choice is informed by the the statistical quality of the fit, we also introduce physical interpretations of the data in order to help categorize our sample. Therefore, although for many galaxies the choice of model is obvious, the methods for choosing models are not definitive and can be changed to suit the problem at hand. Our main interest is in identifying galaxies with classical ($n_b = 4$) bulges, which is reflected in our method of categorizing galaxies described below.

5.1 $n_b = 1$ vs. $n_b = 4$ Bulges

The obvious metric for choosing the best-fit model for each galaxy is the χ^2 value from the fitter. However, the χ^2 values for different models do not differ greatly, and many of the galaxies have significant structure (spiral arms, rings, etc.) that is poorly fit by the models, leading to large values for χ^2. Thus, we require additional information. Instead of relying on statistical tests alone, we categorize galaxies by using a series of tests similar to the logical filter employed by Allen et al. (2006). As in their work, our default choice will be a single component Sérsic model. We first separate out the galaxies which statistically are best fit by single component exponential or de Vaucouleurs profile. In addition, we compare the disk and bulge components of the B+D fits to the exponential and de Vaucouleurs fits. If the 2-component fits and 1-component fits are the same to a chosen tolerance (i.e. either the bulge or disk flux is consistent with zero), we model the galaxy with a single component. Finally, we divide the galaxies into $n_b = 4$ and $n_b = 1$ bulges, using the colours and axis ratios of the bulges.

(i) *Exponential disk profiles:* The easiest category to find is the pure disk galaxies. Because exponential disks are used in both B+D models, these models and the pure exponential model yield similar results for pure disks. The first criterion we use to select pure disk galaxies is the statistical significance of the bulge component. We do this by comparing the (non-reduced) χ^2 value of the B+D fits to the χ^2 from single component exponential disk fits. Since the B+D fits contain more parameters, the quality of the fit should improve and the χ^2 of the fit should decrease. For linear models fit to
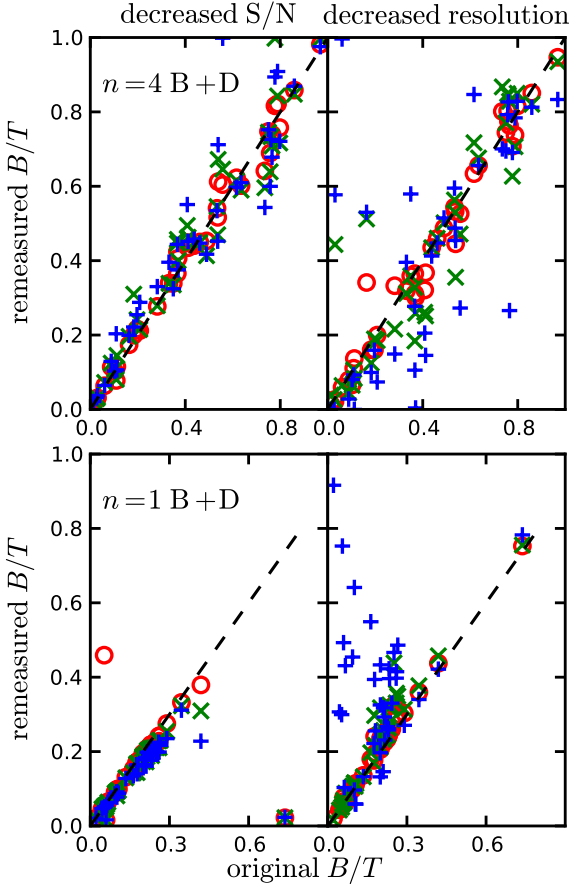
Figure 9. Change in B/T with decreased S/N(left) and resolution (right) as a function of B/T measured in the non-degraded images for Sample A galaxies. The symbols are as in Figure 5.

Figure 10. Change in measured bulge $R_{\rm eff}$ for the $n_b = 4$ B+D models (top) and $n_b = 1$ B+D models (bottom) as a function of bulge $R_{\rm eff}$. The left(right) column shows trends with decreased S/N(resoltuion). The symbols are as in Figure 5.

data with Gaussian errors, the expected difference in χ^2 can be quantified (Lupton 1993). The B+D model fits an image with n pixels using 10 free parameters. An exponential disk uses the same model, but fixes the bulge parameters, thus increasing the numbers of degrees of freedom by 4. If these were linear models, the difference of the χ^2 for the models, $\chi^2_{\rm exp} - \chi^2_{\rm B+D}$ would be independent and follow a χ^2 distribution for 4 degrees of freedom. The relevant statistic is

$$f = \frac{\left(\chi^2_{\rm exp} - \chi^2_{\rm B+D}\right)/4}{\chi^2_{\rm B+D}/(n-10)} \quad , \qquad (4)$$

where f follows an $F_{4,n-10}$ distribution (see Lupton 1993). If f is large, there is a low probability of the difference in χ^2 occurring due to the additional degrees of freedom alone. Although our models are not linear and our errors are only approximately Gaussian, we require that f be larger than the 99.99% level from the $F-$distribution. This ensures that the bulge is a statistically significant part of the fit. We compare the exponential fit to each B+D fit separately, and assign galaxies for which neither bulge is statistically significant to the exponential disc category. There are $5,893$ galaxies which satisfy this criterion. However, we would also like to include galaxies for which the bulge may be formally statistically significant, but for which the bulge is small compared
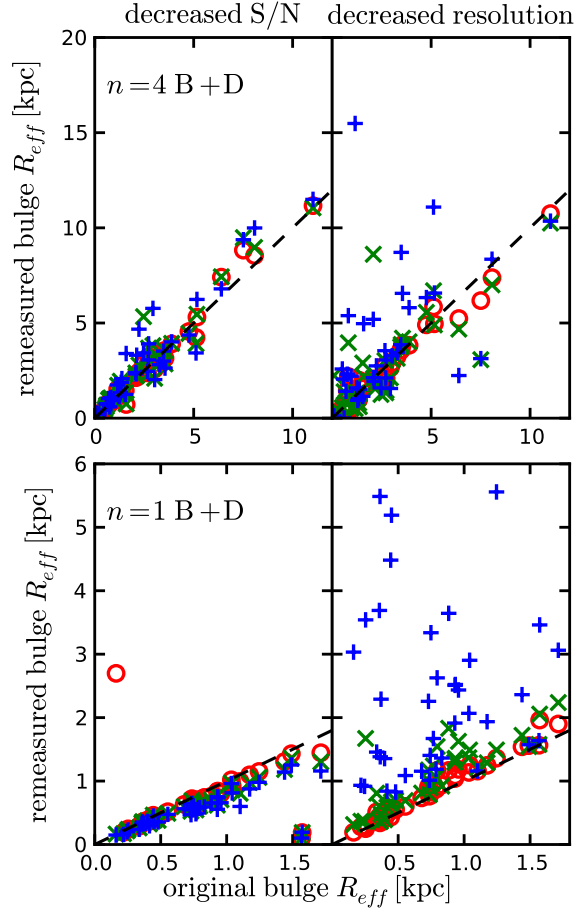
to the systematic errors examined in the sections above. In order to do this, we select galaxies for which the disk in the B+D model matches the single exponential fit in total flux, axis ratio (q_d), and $R_{\rm eff}$ to within 10%. When these galaxies are included in the sample, there are 15438 pure disk galaxies. Only 2.6% of the 5893 galaxies which pass the first (statistical) test, fail the second test.

(ii) *de Vaucouleurs profiles:* The initial procedure to select de Vaucouleurs, or elliptical galaxies is similar to that used for exponential galaxies. However, in this case we can only directly compare the single de Vaucouleurs profile fit to the $n_b = 4$ B+D model. First, we select 755 galaxies for which the difference in χ^2 values for the de Vaucouleurs model and the $n_b = 4$ B+D model is not statistically significant. The 4 galaxies which satisfy both the conditions for a de Vaucouleurs profile and an exponential profile are removed from both lists, and fit by a single Sérsic component instead.

We expect the number of elliptical galaxies in our sample to be much larger than 755. The reason this number is so low can be seen in Figure 2d. Many elliptical galaxies are well fit by an $n_b = 4$ bulge and a large, low surface brightness disk. Because the disk has a large scale length, the measured B/T can be as low as $\sim 40 - 50\%$. This has been found in other
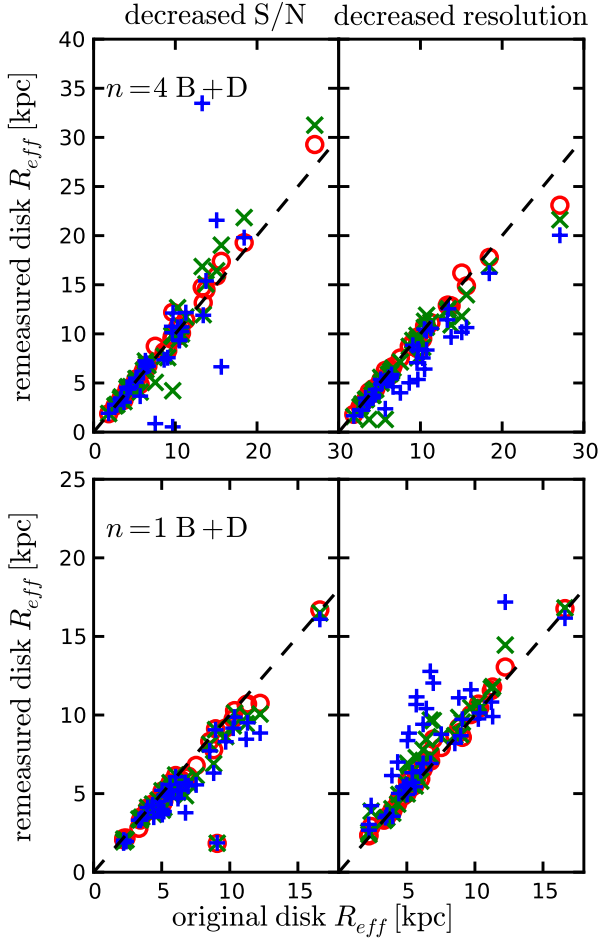
Figure 11. Same as Figure 10 for the disk R_{eff}s.

Figure 16. Change in r-band magnitude with increasing redshift as a function of Sérsic index for Sample A galaxies. The symbols are as in Figure 5, with the red circles, green ×s and blue crosses representing a decrease in angular size by a factor of 2, 4, and 10, respectively. These plots can be compared directly to the results in Figure 7.

studies (Allen et al. 2006), and is typically not interpreted as a low luminosity disk, but rather as an extended halo, a second Sérsic component (Gonzalez et al. 2005), tidal features, or a Sérsic index that is larger than 4. This feature could also be due to uncertainties in the sky in the vicinity of bright, extended objects, although the new DR8 reductions attempt to reduce these uncertainties. From the 755 galaxies above, we find that 90% of them have $g - r > 0.55$ and $g - i > 0.8$, and $b/a > 0.55$. In order to find elliptical galaxies, we select galaxies which satisfy these three criteria using the de Vaucouleurs models. These galaxies all lie on the red sequence, but not all galaxies on the red sequence are ellipticals (Bundy et al. 2010), and S0 galaxies should be modeled as B+D galaxies. Therefore, we must also examine the two component fits for these red sequence galaxies. Typically, ellipticals in our sample are well fit by 2 round $n = 1$ Sérsic components, or by a large $n_b = 4$ bulge and a very large, low surface brightness exponential component. If the galaxies along the red sequence have an $n_b = 1$ B+D fit with a round ($q_d > 0.4$), red ($g - r > 0.65$) disk, and have an $n_b = 4$ B+D fit with a large ($B/T > 0.4$), red ($g - r > 0.65$) , round ($q_b > 0.55$) bulge, we assume they are elliptical galaxies and fit them with single component de Vaucouleurs model. This category contains 9692 galaxies. Figure 19 shows the axis ratio distribution for the $n_b = 4$ B+D models for the de Vaucouleurs galaxies. If these galaxies were dominated by
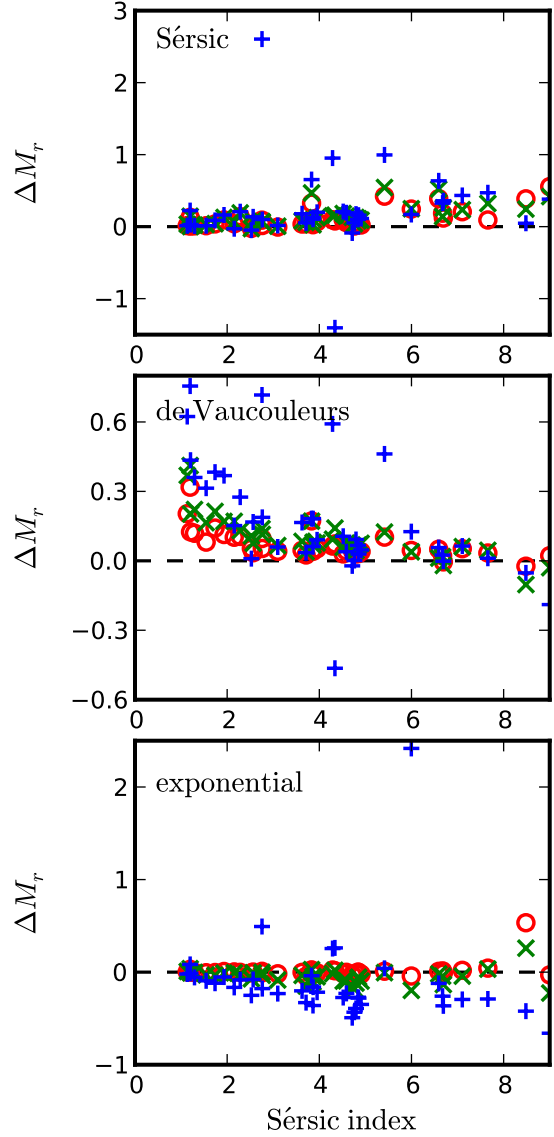
S0 galaxies with real disks, the q_d distribution would be flat. Instead, the distribution is biased to high values of q_d with a peak at $q_d \approx 0.75$.

(iii) *bulge + disk:* After removing all galaxies which are best-fit by a single exponential or de Vaucouleurs profile, there are 46,155 galaxies remaining. Among these galaxies, we select only those which have physically sensible bulge and disk parameters for both models. We require that the bulges and disks in both models are detected in g,r,and i-band images. This eliminates 6366 galaxies. We also require that the bulges and disks are arranged in the expected manner, i.e. the bulge R_{eff} is smaller than that of the disk and the bulge flux dominates in the central part of the galaxy. This leaves 24,974 galaxies.
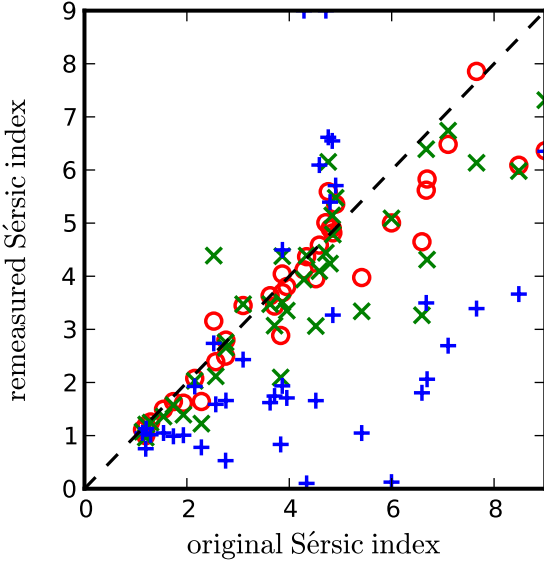
Figure 17. Comparison of the Sérsic index measured for redshifted Sample A galaxy images to the Sérsic index measured for the original Sample A images. The symbols are as in Figure 7.
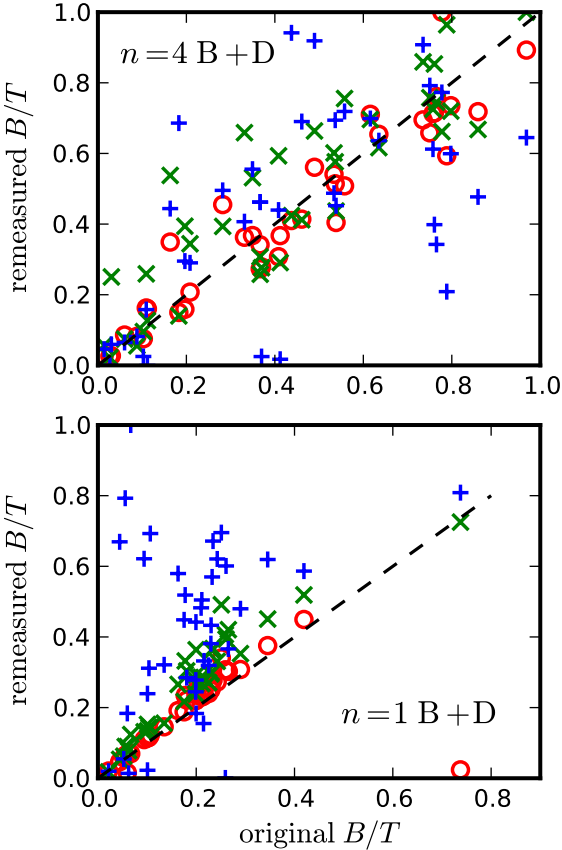

Figure 18. Comparison of the B/T measured for redshifted Sample A galaxy images to the B/T measured for the original Sample A images. The symbols are as in Figure 7.
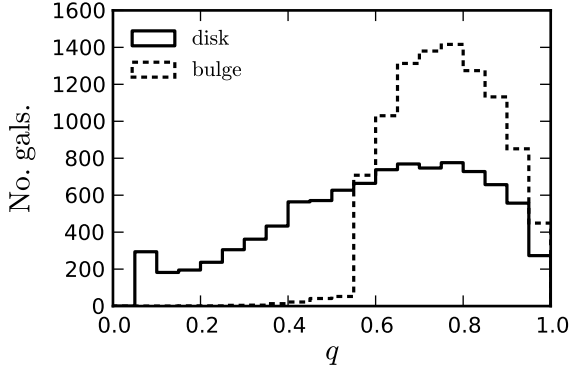

Figure 19. Distribution of $n_b = 4$ B+D bulge and disk axis ratios for the $9,692$ galaxies best fit with a single component de Vaucouleurs model.

At this point, we must distinguish between galaxies with classical, $n_b = 4$ bulges and pseudo-bulges ($n_b = 1$). For most galaxies, the χ^2 values for the fits do not differ significantly. From the χ^2 values for the fits, we can calculate the probability that a model is a good fit using equation 3. For Gaussian errors, the expected probability value for a good fit is 50%; a value near 0 represents a poor fit, while a value near 100% suggests the model over-fits the data, or the errors are underestimated. Only 6% of the galaxies have B+D model fits with probability values between 5 and 95%, suggesting that the χ^2 value is not useful for discriminating between B+D models.

The distributions of bulge colours and inclination angles for all B+D galaxies fit with both models are shown in Figure 20. The colour distributions for bulges peak around $g - r \sim 0.8$, which lies along the red sequence, but there is an excess of bulges blue-wards of 0.8. The existence of this excess was also found by Allen et al. (2006). The expectation is that pseudo-bulges should be disk-like ($n = 1$ profiles) (Fisher & Drory 2008) and have ongoing star-formation (Fisher 2006; Kormendy & Kennicutt 2004). Therefore, instead of relying on the statistical properties of the fits, we categorize bulges by their shape and colour. We expect classical bulges to be red and round, compared to their disks. If the $n_b = 4$ bulge component has $g - r > 0.6$ and $q_b/q_d > 0.65$, we model the galaxy with an $n_b = 4$ bulge. Otherwise, if the $n_b = 1$ bulge and disk have similar axis ratios ($0.5 < q_b/q_d < 2.0$), we categorize the galaxy as a pseudo-bulge ($n_b = 1$) host. This leaves a sample of 14042 $n_b = 4$ B+D galaxies and 6684 $n_b = 1$ B+D galaxies. The remaining $4,275$ galaxies are placed in the Sérsic profile category. The exact choice for the axis ratio and colour cutoffs for this sample is somewhat arbitrary, and changing the values will change the categories for some galaxies. The division above is somewhat conservative as it places a significant fraction of the galaxies into the Sérsic category.

Our models do not include a separate bar component and we expect light from the bar to typically be included in the bulge. Barred galaxies are distinguished by bulges with small axis ratios compared to their host disk. Therefore, barred galaxies are categorized either as $n_b = 1$ B+D galaxies (for weak bars) or Sérsic galaxies. The 3963 galaxies with bulges significantly flatter than their disks (i.e., bars) are placed in
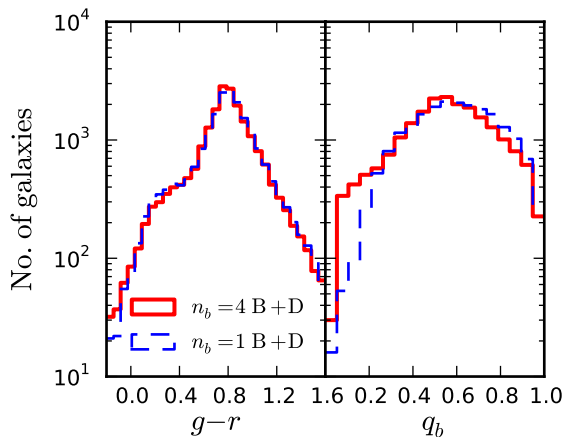
Figure 20. Distribution of bulge colours and axis ratios for all 20,726 B+D galaxies, fit with both B+D models.

the Sérsic profile category. Of these barred galaxies, around 1/2 have red bulges/bars.

(iv) *Sérsic profile:* We use the Sérsic profile for galaxies which do not fit in any of the categories above. This group includes 25,970 galaxies, and is the largest category. Of the galaxies in this group, 40% do not have χ^2 values which are significantly improved by adding a second component to the Sérsic fit. The distribution of Sérsic indices and magnitudes for this group are shown in Figures 21 and 22. The median Sérsic index for these galaxies is $n = 1.5$, suggesting these galaxies are disk-like rather than ellipticals. Furthermore, the galaxies fit with Sérsic profiles are intrinsically fainter than the majority of our sample; the median r-band absolute magnitudes differ by 0.5 magnitudes. These galaxies also have a median $g - r$ colour 0.1 mag bluer than the entire sample. All of this suggests that a large fraction of the Sérsic profile fit galaxies are faint, star-forming, disk-like (or irregular) galaxies for which a B+D model is a poor choice.

We have evaluated our category assignments by visual inspection on Sample B, a subset of 265 randomly selected galaxies. Of the 51 galaxies classified as exponential disks, $\lesssim$ 6% are too irregular to obviously identify a disk. Of the 50 de Vaucouleurs galaxies, 7 should be classified as B+D galaxies. There are 19 $n_b = 1$ B+D and 59 $n_b = 4$ B+D galaxies in this sample. The $n_b = 4$ and $n_b = 1$ galaxies are difficult to distinguish by eye, but only $\sim$ 8% (6 galaxies) of the sample can be visually classified as ellipticals. The remaining 85 galaxies are fit with a Sérsic profile. As expected from the Sérsic index distribution in Figure 21, most of these galaxies are disk galaxies, and many nearly edge on, or dominated by a large bar. It makes sense that these types of galaxies are most likely to have a poor quality or unphysical fit for one of the B+D models, and therefore be placed in the Sérsic category. Additionally, the Sérsic-fitted galaxies are fainter than the B+D galaxies, with a median SDSS model r-band magnitude of 16.7 compared to 15.9 for the $n_b = 4$ B+D galaxies.

In addition to visual inspection for a small sample, we have also examined the statistical properties of the whole sample. Figure 22 shows the fraction of galaxies in each category as a function of apparent and absolute magnitudes.
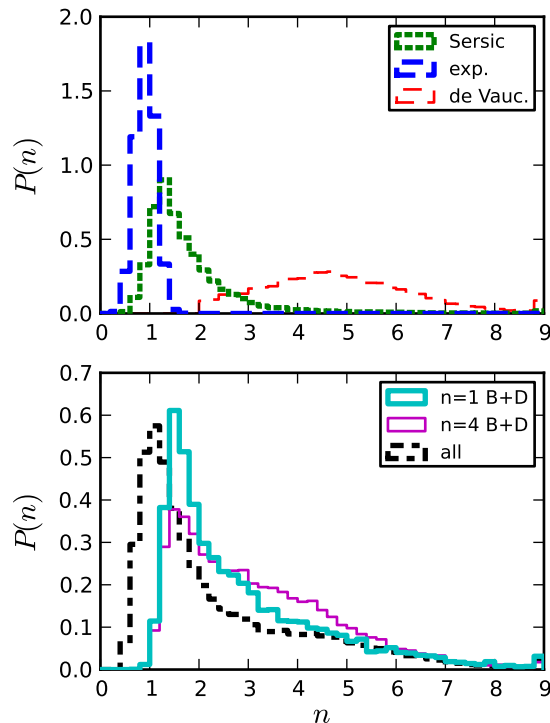

Figure 21. Distribution of Sérsic indices (from the single component Sérsic fits) for the galaxies in different categories. The galaxies are placed in the five categories according to the alogrithm described in §5.1. Note the different scales in the two plots.

Unsurprisingly, de Vaucouleurs galaxies (ellipticals) dominate the bright end of the sample. At the faint end, 50% of the galaxies fainter than $\sim$ 17 in r are placed in the Sérsic fit category, suggesting that B+D fitting becomes difficult for faint galaxies. The absolute magnitude distribution shows that the intrinsically faintest galaxies in our sample are typically categorized either as exponential disks or Sérsic fit galaxies. This is in agreement with observations that intrinsically faint galaxies are more likely to be disorganized, and therefore more difficult to fit with a B+D model than brighter galaxies. The rightmost panel in Figure 22 shows the fractional distributions of absolute magnitude for the 43,403 galaxies brighter than 16.7 in r. This distribution is not significantly different than that for the total sample; only the fraction of exponential galaxies decreases. This demonstrates that the high fraction of Sérsic modeled galaxies at low luminosity is due in large part to the intrinsic nature of these galaxies, and not just the inability of the fitter to fit B+D models to apparently faint galaxies. Thus, our fitter and categorization algorithm successfully identify B+D galaxies in our sample. The galaxies which default to a Sérsic profile are most likely disorganized, intrinsically faint galaxies for which a B+D model is inaccurate. Finally, we note that the shape of the absolute magnitude distribution for the intrinsically bright sample (lower right panel) is different from the absolute magnitude distribution for the whole sample, which should not be the case for a truly magnitude-limited sample. However, our sample also includes a volume (redshift) limit which affects the distribution of bright
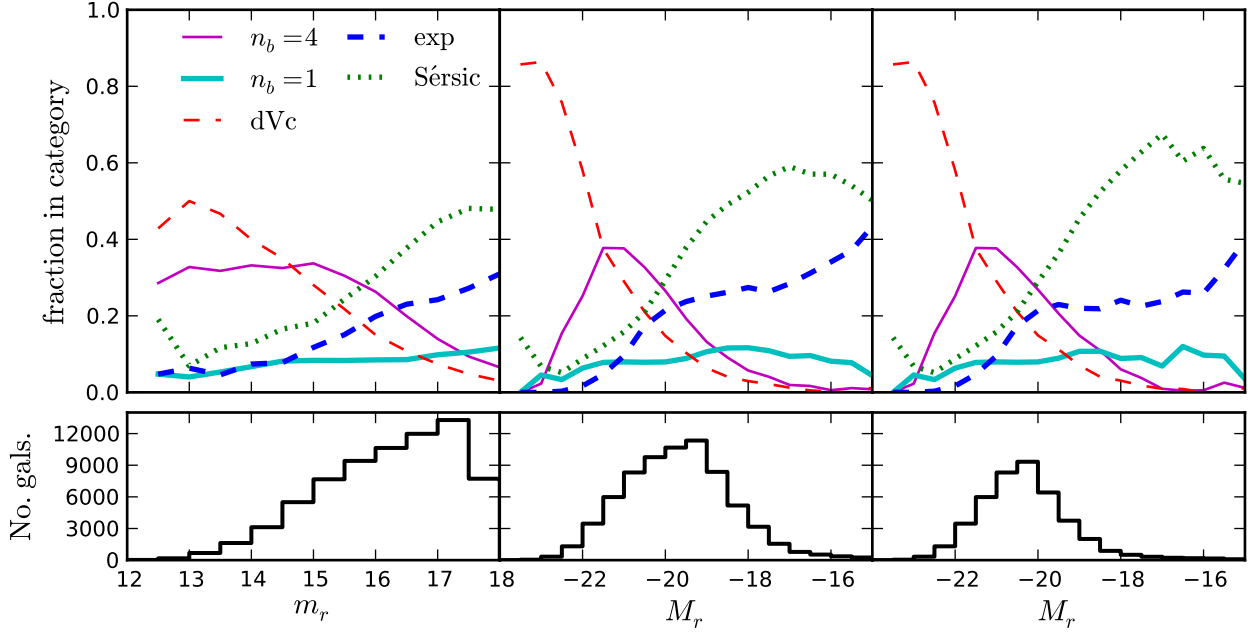
Figure 22. Top panels: Fraction of galaxies in each category as a function of apparent magnitude (left) and absolute magnitude (middle and right). Lower panels: Apparent and absolute magnitude distributions for the sample in each of the top panels. The rightmost column shows galaxies with $m_r < 16.7$.

galaxies, and we do not expect the distribution of absolute magnitudes to scale simply.

Figure 21 shows the distribution of Sérsic indices for a single component fit for the different categories. As expected, exponential disk galaxies have $n \approx 1$, while de Vaucouleurs galaxies have $n \gtrsim 2$ (by selection), and a wide distribution of Sérsic indices peaking at ~ 4.5. The B+D modeled galaxies both have peaks in their Sérsic index distributions near $n \approx 2$, but the $n_b = 4$ B+D galaxies tend to have slightly higher Sérsic indices for the whole galaxy than the $n_b = 1$ B+D modeled galaxies.

5.2 Comparison to Other Studies

Gadotti (2009)(G09) have performed bulge-bar-disk decompositions on a sample of ~ 1000 SDSS galaxies, selected to give high quality model fits. We have matched their sample to ours and found 442 matches. Eighty percent of the remaining galaxies in their sample are outside our redshift range. K-correcting our magnitudes to $z = 0.1$, we find excellent agreement between the model magnitudes, with the mean $\Delta M_r = -0.11 \pm 0.25$. In galaxies for which we both measure disks, the scale lengths also agree well, although ours are systematically larger, with a median difference of 8%. In comparing the B/T, we find that our measured B/T is systematically larger by 22%. This is not surprising, since G09 include a bar component in their models and we do not, which will substantially affect the bulge (Gadotti 2008). If we compare our B/T to their B+Bar/T, we find no offset, although the inter-quartile range of (B/T)−(B+Bar/T) is [−34%, 58%]. This helps confirm that our bulges include bars. Similarly, our bulge effective radii differ significantly. Because we set the Sérsic index of the bulge to either 4 or 1,

Table 1. Table comparing G09 categorizations to this work. The rows show the G09 categorizations and the columns show this works categorizations.

	classical	pseudo	elliptical	no bulge	total
$n_b = 4$ B+D	46	12	11	0	69
$n_b = 1$ B+D	39	15	1	0	55
de Vauc.	103	2	84	0	189
exp. disk	5	42	0	4	51
Sérsic	22	45	4	7	78
total	215	116	100	11	442

our classical bulges typically have larger scale lengths and our pseudo-bulges typically have smaller scale lengths than those in G09. In comparing our classification to G09 (see Table 5.2), we find that our use of 2 component fits is more conservative. Most of the galaxies we classify as classical bulges G09 does as well. However, almost half of the galaxies G09 classifies as classical bulges, we classify as ellipticals. Similar trends, although less robust, hold for the classification of pseudo-bulges and pure disk galaxies. The fraction of Sérsic galaxies we find in the G09 sample is lower than that in our complete sample. This is due to the fact that G09 have more carefully selected their sample for galaxies which can support a B+D model.

We have also compared our sample to the larger sample from S11. There are $67,333$ galaxies which are fit in both samples; the missing galaxies are the brightest in our sample which the S11 sample excludes. The S11 work fits each galaxy with three models and uses an F−test to determine whether a bulge+disk model is needed. A galaxy is fit with a bulge+disk if there is less than 32% chance that a single Sérsic profile is a better fit. This threshold

is much higher than the one we set for the F-test in §5.1, which leads to more galaxies fit with a bulge+disk model in the S11 sample. Nonetheless, the results of their $F-$test compare favorably to our division into galaxies with bulges and disks. Seventy-five percent of the galaxies we fit with a $n_b = 4$ bulge+disk also pass their $F-$test, while only 23% of our Sérsic-modeled galaxies are better fit with a bulge+disk model according to S11. However, we find poor agreement between the S11 $F-$test and our categorization of elliptical galaxies; fifty percent of the galaxies we fit with a single de Vaucouleurs profile have a disk component according to S11. This is probably due to our inclusion of galaxies with large, low luminosity disks in the elliptical galaxy category. Finally, S11 find that the SDSS images are typically not of high enough resolution to determine the Sérsic index of the bulge, in agreement with our conclusions above.

We also compare the measured parameters for galaxies from S11 to our sample. We limit the comparison to the $\sim 10,000$ galaxies that both studies assign a $n_b = 4$ bulge+disk model, and find reasonable agreement for all the model quantities. The r-band magnitudes found by S11 are systematically 0.06 magnitudes brighter, which is due to differences in the cutoff radii and the sky subtraction. There is no offset in disk scale lengths between the studies, and the scatter $(\mathrm{RMS}[(R_{\mathrm{this\ work}} - R_{S11})/R_{\mathrm{this\ work}}])$ is 11%. The differences between the bulge scale lengths are larger. The bulge scale lengths we measure are 17% larger on average than those in S11, and the scatter is 50%. However, the B/T ratios we find are only 2% larger on average, with a scatter $(\mathrm{RMS}[B/T_{\mathrm{this\ work}} - B/T_{S11}])$ of 0.1. The fluxes are more robust than the scale lengths and the differences in bulge and disk colors are similar to the differences in B/T.

5.2.1 Kormendy Relation

Unlike classical bulges, pseudo-bulges are not expected to lie on the fundamental plane. In fact, the difference in the Kormendy relation (Kormendy 1977) for classical and pseudo-bulges can be used to identify pseudo-bulges (G09). Figure 23 shows the Kormendy relation for ellipticals and bulges in our sample. The solid line shows the relation fit to the ellipticals (red contours), which has the equation: $\langle \mu_{R_{\mathrm{eff}}} \rangle = (2.27 \pm 0.04) \log R_{\mathrm{eff}} + (12.18 \pm 0.15)$, which agrees with the Kormendy relation for SDSS galaxies (Bernardi et al. 2003). The central contours for the classical ($n_b = 4$) bulges lie along the same relation as the elliptical galaxies (at smaller radii), while the $n_b = 1$ B+D form a steeper relation, and the majority do not lie on the elliptical galaxy Kormendy relation. This supports or use of colour and shape as a discriminator between classical and pseudo-bulges.

5.3 Inclination and internal extinction

Just as we must correct for extinction from our own galaxy, the colours and magnitudes in our sample should be corrected for internal extinction from the sample galaxies themselves. Since elliptical galaxies contain little dust, they are not affected by intrinsic extinction, while disk galaxies become redder and fainter with increasing inclination (Burstein et al. 1991). Additionally, even if bulges contribute nothing to the extinction themselves, their light will be attenuated by the encompassing disk.
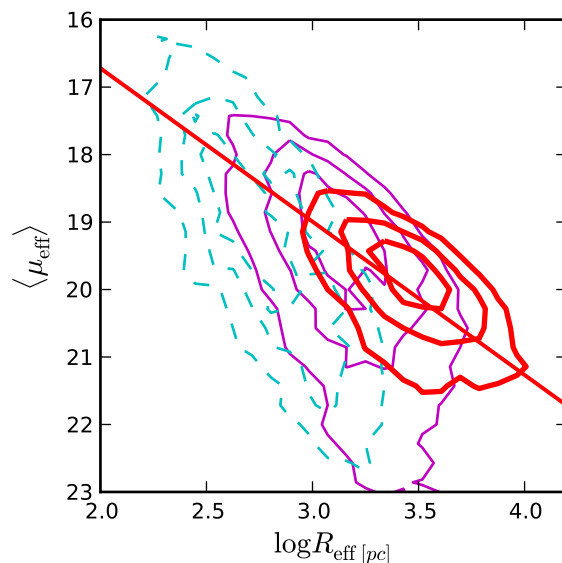

Figure 23. Kormendy relation for bulges of $n_b = 4$ B+D (thin solid, magenta), $n_b = 1$ B+D (dashed, cyan) and de Vaucouleurs(thick solid, red) modeled galaxies. The straigt line is a fit to the binned medians of the elliptical galaxies, and is given by the formula $\langle \mu_{\mathrm{eff}} \rangle = (2.27 \pm 0.04) \log R_{\mathrm{eff}}[\mathrm{pc}] + (12.18 \pm 0.15)$. The contours enclose 30%, 50%, and 80% of each category.

Before correcting for inclination, we examine the distribution of inclination angles of disks in our sample. These are shown in Figure 24. The dotted line is the theoretical distribution of axis ratios, assuming a disk flattening of $1/q_z = 5$. The measured axis ratio and its probability density function are

$$q_d = \sqrt{q_z^2 + (1 - q_z^2)\cos\theta}\ , \text{ and} \qquad (5)$$
$$P(q_d) = q / \left[\sqrt{(1 - q_z^2)(q^2 - q_z)^2} \right]\ ,$$

where θ is the inclination angle. Figure 24 shows that our sample is missing galaxies face-on ($q_d = 1$) galaxies, which is not surprising since any intrinsic asymmetry in the galaxy will decrease the measured axis ratio. Additionally, the lower panel shows that the distribution of disk angles depends on the profile used for the bulge. The thick lines show the distributions of disk axis ratios for the *same* set of galaxies using an $n_b = 4$ and an $n_b = 1$ B+D model. The measured disk axis ratio tends to be higher (less inclined) for the $n_b = 1$ B+D models. We have examined a set of galaxies for which the difference in measured inclination angle for the two B+D models is large. Many of these galaxies are edge-on disks with prominent bulges. These galaxies are poorly fit by the $n_b = 1$ B+D models, as the disk and bulge have the same profile shape and are easily confused. Nonetheless, because our $n_b = 1$ versus $n_b = 4$ bulge separation relies on colour, and highly inclined disks will lead to redder colours, we will re-categorize the B+D galaxies, using inclination-corrected bulge colours.

The internal extinction correction can be divided into two parts, the increase in extinction due to inclination, and the extinction due to dust in face-on galaxies. The former portion can be corrected by removing trends in galaxy properties with inclination (Tully et al. 1998; Driver et al. 2007; Shao et al. 2007; Maller et al. 2009). Driver et al. (2007)
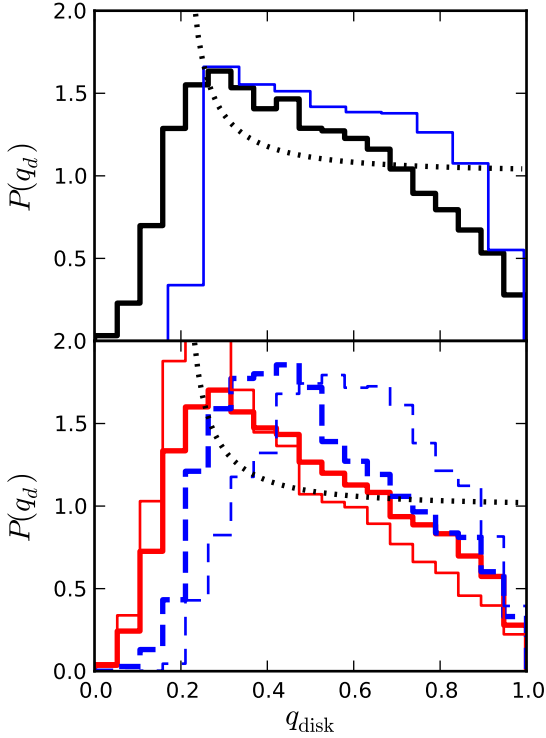
Figure 24. Distribution of disk axis ratios. The dotted line in both panels show the expected distribution for a constant disk flattening of 5. Top panel: The thick black line is the distribution for all disks (from exponential and B+D galaxies). The thin blue line is for single component exponential fits. Bottom panel: The thick red, solid (blue, dashed) line is for all the B+D galaxies fit with an $n_b = 4$ ($n_b = 1$) B+D model. The thin lines of the same colour/style only show the galaxies which were categorized as $n_b = 4$ B+D or $n_b = 1$ B+D.

and Driver et al. (2008) have derived extinction corrections for bulges and disks separately using B+D decompositions of the Millennium Galaxy Catalogue (Liske et al. 2003). Their magnitude corrections also include a face-on attenuation. In this work, we will only address the inclination dependent portion of the internal extinction. In order to compare the properties of classical bulges in this sample to elliptical galaxies, we will be required to address face-on attenuation, but in comparing the properties of bulges to other bulges, it is not necessary. In order to correct the colours for inclination effects, we use the corrections derived by Maller et al. (2009)(M09). These corrections are derived by removing trends in $\lambda - K$ colours with axis ratio (q). The corrections to the $\lambda - K$ colours are of the form

$$A_{\lambda - K} = -\gamma_\lambda \log q \quad \text{where} \qquad (6)$$
$$\gamma_\lambda = \alpha_o + \alpha_K (M_K + 20) + \alpha_n n_{\text{Sersic}} \, ,$$

where M_K is the extrapolated K_s−band magnitude from 2MASS (Jarrett et al. 2000). The fitting constants α_x can be found in Table 2 of M09. Just over 50% of the galaxies in our sample can be matched to a 2MASS object. For the remainder of the objects, we can estimate M_K from the SDSS model i-band magnitude and $r - z$ colour as:

$$M_K = 1.66 + 1.07 \times M_i - 0.94 \times (r - z) \quad , \qquad (7)$$

which is derived by a least-squares fit to an apparently bright ($m_r > 15.7$) sample of galaxies with 2MASS data. The rms scatter around this relation is less than 0.002 magnitudes. Below, we examine the correction applied to galaxies with and without K-band observations separately. We have also tested our inclination correction on a bright ($m_r > 15.7$) sample of $\sim 23,000$ galaxies, of which 95% have K-band observations. These galaxies are on average redder than the rest of our sample, but the results of the inclination correction remain the same.

The inclination corrections in M09 were derived using a sample of ~ 8000 disk-dominated galaxies from SDSS, most of which are included in our sample. These corrections were derived for galaxies fit with a single Sérsic profile. For our sample of B+D fits, we apply a correction both to the bulge and the disk, separately. We use the single component Sérsic fit for n_{Sersic}, the total K−band magnitude (or an estimate), and the measured disk inclination angle for the correction. Because we use the disk inclination instead of the total galaxy inclination, we find that the M09 $A_{\lambda-K}$ over-corrects the disk colours in our sample, both for bulge-less galaxies and galaxies with bulges. We have adjusted the corrections for this by removing trends in disk colour with inclination. Additionally, we have assumed that only $1/2$ the bulge light is extincted by the disk. Our justification for this is the assumption that the bulge light extends well above the disk, gas, and dust. Therefore, if all the extinction occurs in the the plane of the disk, a reasonable assumption, a significant fraction of the bulge light will not be extincted, and the bulge correction should reflect this. The form the the fractional bulge correction is

$$A_{\lambda - K}(\text{bulge}) = 2.5 \log \left(0.5 \left(1 + 10^{0.4 A_{\lambda - K}(\text{disk})} \right) \right) \, . \qquad (8)$$

The M09 inclination correction applied to our sample of pure disk galaxies is shown in the first two panels of Figure 25. These panels show that the M09 corrections over-correct inclined disks. They also show that the distribution of $g - r$ colours for galaxies without K-band observations is bluer than that for galaxies with K-band observations (about $1/3$ of disk galaxies). This makes the difference between inclined an face-on galaxy colours small. Indeed, the difference in median colour between between inclined galaxies and face-on galaxies without K is less than 0.1 mags.

The over-correction of disk colours using M09 also occurs for disks in B+D modeled galaxies. This over-correction is partially due to the fact that we use the disk inclination instead of the total galaxy inclination in the equation 6. We correct for this by removing trends in disk colours with $\log q_d$, adjusting the α_0 term in equation 6. We use our sample of pure disk galaxies, including galaxies with and without K-band observations. We have chosen to correct colours including i-band because the M09 correction works best for the i-band (among g, r, and i). This is evident from the trend in $i - K$ with the K-band magnitude for disk galaxies. The M09 correction aims to remove trends in this relation with $\log q_d$; examining our data, the trend with the slope of the relation between $i - K$ and K is smaller than that for g and r. Given this choice, the i-band α_0 does not change. For the u, g, r, and z bands, the values -0.302, -0.183, -0.089, and 0.050 are added to α_0. The results of this change to α_0 are shown in the right two panels of Figure 25, for galaxies with large ($q_d < 0.4$) and intermediate ($0.4 < q_d \leqslant 0.55$)
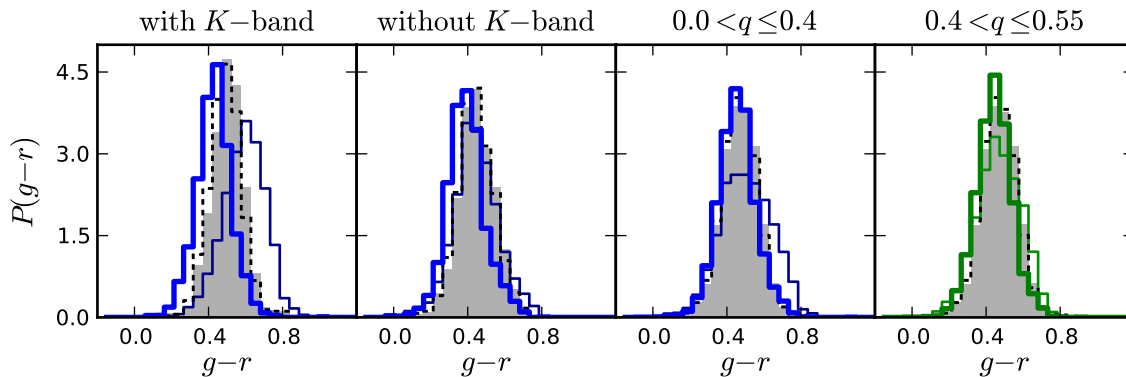
Figure 25. Corrected colour distributions for galaxies fit with a single exponenital profile. In all panels, the shaded region shows the uncorrected colour distribution for face-on ($q_d > 0.85$) galaxies, the black dotted line shows the corrected colour distribution for face-on galaxies. In the first three panels, the thin and thick blue lines show the uncorrected and corrected colours for edge-on ($q_d < 0.4$) galaxies. In the last panel, intermediate inclination galaxies ($0.4 < q_d \leqslant 0.55$) are shown. The first two panels show the M09 correction applied to galaxies with and without K band data. The final panels show all the disk galaxies using the M09 correction plus our adjustment for the over correction.

inclinations. The medians of the corrected colour distributions for inclined galaxies are still ~ 0.01 mag too blue, but this should be compared to the ~ 0.05 mag offset in colour for the uncorrected M09 inclination corrections.

Figures 26 and 27 shows the inclination correction applied to B+D fitted galaxies. Here, the corrections include our modifications, and the bulge correction is given by equation 8, which only extincts 1/2 the bulge light. For the $n_b = 4$ B+D galaxies, the bulge and disk corrections work reasonably well for galaxies with large and intermediate inclinations. If instead of correcting 1/2 the bulge light, we correct all of it, the median corrected $g - r$ of the most inclined galaxies is 0.02 magnitudes bluer than the median colour of bulges in face-on galaxies, while they agree to 0.002 magnitudes when only corrected 1/2 the bulge light. The distribution of bulge and disk colours for $n_b = 1$ galaxies are not as successful. For these galaxies, the bulge colours are under-corrected, on average, while the disk colours are over-corrected. This is especially true for galaxies without K-band data. Like the exponential disks without K-band observations, these galaxies have blue disks ($g - r \approx 0.4$) no matter what the inclination angle, and are probably not greatly affected by dust or extinction. For the $n_b = 1$ bulges, the colour distribution is wide, especially for inclined disks (see Figure 26, upper right panel). Some of this spread is due to uncertainties in the bulge colours for small bulges. The $n_b = 1$ B+D galaxies are intrinsically fainter than the $n_b = 4$ B+D galaxies (median M_r of -19.4 versus -20.4), which further implies they will be less affected by dust and the relation between colour and inclination will be weaker.

Using the colour corrections from this section, we can redo the categorization from §5.1. This does not affect the results greatly. In the whole sample, about 200 galaxies are recategorized. For the most part, galaxies are removed from the de Vaucouleurs category and placed in the B+D and Sérsic categories. The $n_b = 4$, $n_b = 1$, and Sérsic categories grow by 39, 64 and 48 galaxies, respectively.
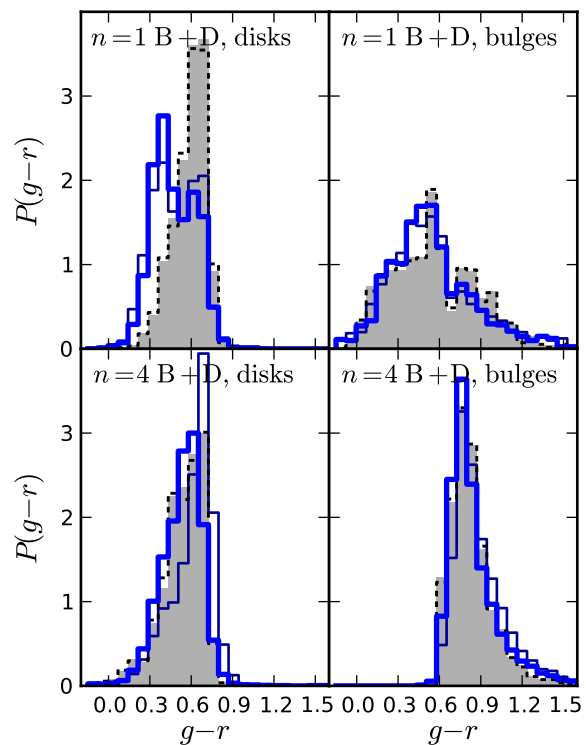

Figure 26. Corrected and uncorrected colour distributions for galaxies fit with $n_b = 1$ B+D models (top) and $n_b = 4$ B+D models (bottom). The thick and thin blue lines show corrected and uncorreted distribtuions for galaxies with $q_d < 0.4$. The shaded region and the black dotted lines show the distributions of uncorrected and corrected colours, respectively, for galaxies with $q_d > 0.85$.

5.4 AGNs

Because we have chosen to fit the entire low redshift, spectroscopic `VAGC` catalogue, our sample contains nearby active galactic nuclei (AGNs). If an AGN is sufficiently bright, it may contaminate the B+D fit, especially the colours of
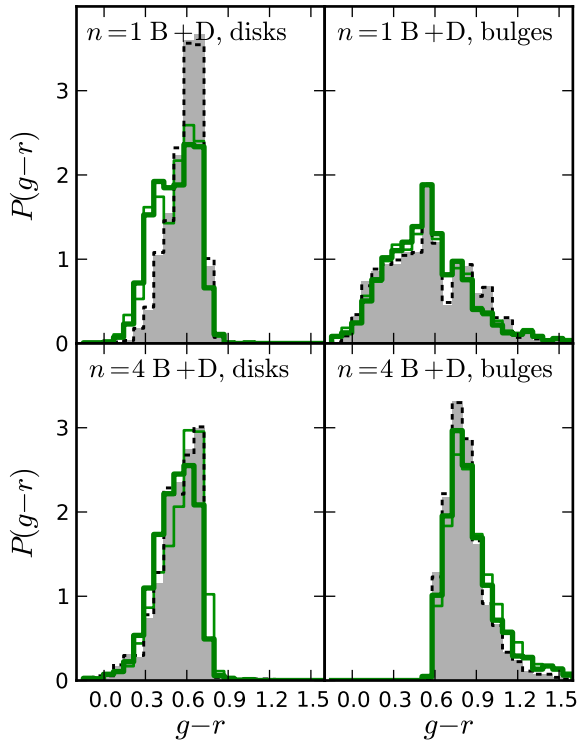
Figure 27. Same as Figure 26, but for galaxies with intermediate inclinations ($0.4 < q_d < 0.55$).
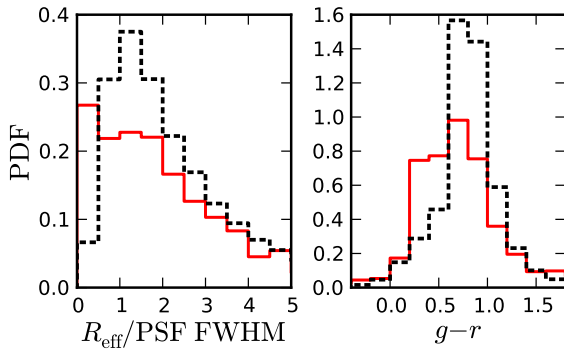

Figure 28. Probability distributions for the $n_b = 4$ bulge R_{eff} and $g-r$ colour for all $B+D$ modeled galaxies (black dotted line) and the 1134 BLAGN from Hao et al. (2005) (red solid line) fit with $n_b = 4$ B+D models. The AGN sample is 1.3% of the whole sample.

the bulge. However, most nearby AGN do not outshine their host galaxy, and the B+D fits and colours will not be greatly affected (Hao et al. 2005; Simmons & Urry 2008). Simmons & Urry (2008) find that the B/T for AGN hosts is systematically over-estimated by $\sim 10\%$, but for weak AGN ($L_{AGN}/L_{host} \lesssim 10\%$), the change in B/T is consistent with zero. Gadotti (2009) find that including a point source (AGN) component in their fits is not statistically significant. Kauffmann et al. (2003) find that, although host galaxies of powerful AGN have undergone more recent star formation, the structural properties of narrow-line AGN hosts and the general early-type galaxy population are the same.

Broad-line AGN, however are associated with a bright, blue continuum source which may contaminate our sample. In order to check on contamination from AGN, we have matched our sample against the (updated) broad-line AGN (BLAGN) sample from Hao et al. (2005)(Strauss, priv. comm.). This is a sample of $10,015$ BLAGN spectroscopically selected from SDSS DR7. Matching these samples gives 1134 galaxies with AGN in our sample, or 1.3%. This is comparable the fraction of galaxies with broad-line AGN Hao et al. (2005) found in their much larger spectroscopic sample. Of these 1134 galaxies, 205 are classified as $n_b = 4$ B+D galaxies and 133 are classified as $n_b = 1$ B+D galaxies. The remaining sample is divided into 54 de Vaucouleurs galaxies, 289 exponential galaxies, and 453 Sérsic galaxies. Figure 28 compares the properties of the BLAGN fitted with an $n_b = 4$ B+D to the sample of galaxies identified as B+D galaxies in §5.1 (also all fitted with $n_b = 4$ B+D models). The median bulge R_{eff} for the BLAGN is $2.2 \times$ PSF FWHM, while for the whole sample it is $1.9 \times$ PSF FWHM. However, both of these values are larger than the HWHM of the PSF, suggesting for the BLAGN sample, the bulge component is not purely based on the AGN. If anything, AGN tend to be hosted in large bulges. Using the $n_b = 1$ models, the median $g-r$ colours of the BLAGN bulges are 0.05 mag bluer than the underlying sample, suggesting some contamination from the AGN. Nonetheless, BLAGN make up a very small fraction of our sample, so our results are not greatly affected by this contamination. BLAGNs are not even the majority of extremely blue bulges, which are dominated by galaxies with dense, central starbursts.

5.5   Proxies for B/T and morphology

Although we have performed B+D decompositions for a large number of nearby galaxies, these fitting methods are time-consuming, and inappropriate for higher redshift, lower resolution data. Therefore, we compare our results to other methods for determining galaxy type and B/T. Two simple measures of galaxy type include the global Sérsic index and the Petrosian concentration, C. As with most studies using SDSS, the concentration is taken as r_{90}/r_{50}, where r_{xx} is the radius of the circular containing 90(50)% of the Petrosian flux. Unlike the B/T or the Sérsic index, concentration measurements do not take seeing into account. However, 99% of the galaxies in our sample have $r_{50} > $ PSF FWHM, so the concentration is not significantly affected by seeing in our sample. For perfect Sérsic profiles, concentration is a function of axis ratio, q, and Sérsic index, n; for $q = 1$ and $n = 4(1)$, $C \approx 3.2(2.4)$ (Blanton et al. 2003).

The top panel in Figure 29 shows the relation of Petrosian concentration to B/T for the B+D fitted galaxies. The Spearman's rank correlation coefficient is 0.73. Fitting a line to the inverse relation (for $B/T < 0.6$), yields

$$C = (1.45 \pm 0.01)B/T + 2.21 \pm 0.004 , \tag{9}$$
$$C = (1.41 \pm 0.02)B/T + 2.22 \pm 0.005 , \text{ for } n_b = 4,$$
$$C = (1.34 \pm 0.02)B/T + 2.22 \pm 0.005 , \text{ for } n_b = 1.$$

None of these relations are as steep as those found by Gadotti (2009), who finds a slope of 1.93. The difference in slope is due to the restriction of their sample to galaxies with $b/a > 0.9$, which typically have lower measured B/T
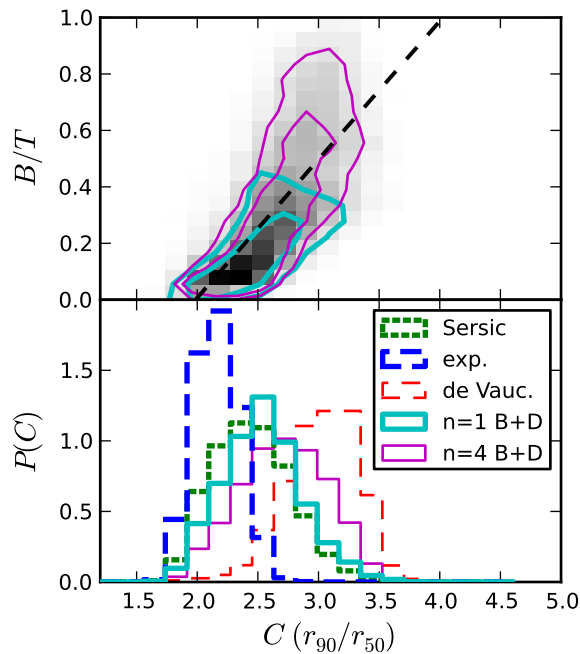
Figure 29. (*Top*): Relation between B/T and Petrosian concentration for the sample of $20,726$ B+D fitted galaxies. The underlying grayscale map includes all galaxies, the thin magenta (thick cyan) contours show the $n_b = 4(1)$ B+D modeled galaxies. The two contours in each colour enclose 50% and 80% of each sample. (*Bottom*): Distributions of Petrosian concentration for the different categories of galaxies.
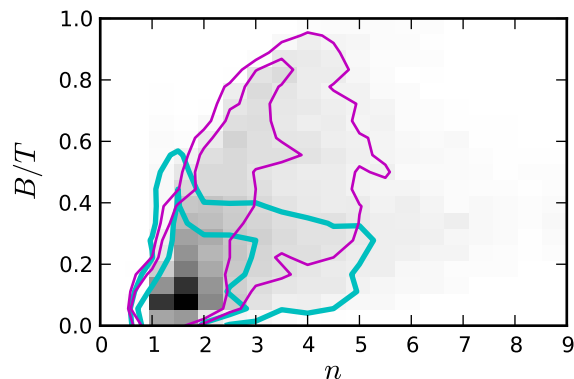

Figure 30. Relation between B/T and the Sérsic index of a single component fit for the B+D fitted galaxies. The symbols are the same as in the top panel of Figure 29.

values. If we restrict our sample to galaxies with $b/a > 0.9$, the measured slope increases to 2.04 ± 0.07. The lower panel in Figure 29 shows the distribution of concentrations for the different galaxy types. Galaxies fit by either an exponential or a de Vaucouleurs profile have well-separated concentrations, centered around 2.2 and 3.1, respectively. B+D galaxies have concentrations in between these values. Figure 30 shows the relation between Sérsic index and B/T; the correlation coefficient is 0.52. The Sérsic index used is that from our single component Sérsic fit, although using the Sérsic index from Blanton et al. (2003) does not significantly change the results. There is a significant scatter to

high Sérsic index for $B/T \approx 0.3$. This is possibly analogous to the two branches of B/T seen for high Sérsic index galaxies in S11. They suggest the scatter is due to poor separation between double and single component galaxies. High Sérsic index models are probably not good fits to the underlying galaxies, highlighting the difficulty in using Sérsic index as a B/T indicator. Like Gadotti (2009), we find that concentration is a better predictor of B/T than Sérsic index.

5.6 Properties of blue, green, and red galaxies

The bimodality of galaxy colours has been well-established both at low redshift (Strateva et al. 2001; Blanton et al. 2003; Baldry et al. 2004) and to $z \approx 2$ (Bell et al. 2004). In optical colours, the bimodal distribution can be modelled as two Gaussian distributions (Strateva et al. 2001; Baldry et al. 2004; Mendez et al. 2011). The minimum between these two distributions, the 'green valley,' is thought to contain galaxies in transition between the red sequence and the blue cloud. The transition occurs as star formation is quenched and different mechanisms for star formation quenching (harassment, ram pressure stripping, AGNs, merging) can have profound effects on morphology. Mendez et al. (2011) have found that the morphological properties of green valley galaxies at $0.4 \leqslant z \leqslant 1$ are intermediate to those on the red sequence and blue cloud, and do not show an enhancement of merger activity, indicating star formation may be quenched by internal processes and less dramatic environmental factors.

Strateva et al. (2001); Driver et al. (2006) show the galaxy colour bi-modality can be traced to the colour bimodality of bulges(ellipticals) and disks, not separate types of galaxies. Figures 31 and 32 show the colour magnitude diagrams for our sample, both for whole galaxies, and galaxies divided into bulges and disks. The colours and magnitudes of bulges and disks have been corrected for inclination. The top panel in Figure 31 shows that ellipticals and pure disk galaxies are well-separated in colour space (this is due in part to the selection of ellipticals based on colour). The bottom panel shows that classical bulge galaxies occupy the green valley, while pseudo-bulge galaxies are predominately blue (as expected from the colour selection of bulges). Figure 32 shows the CMDs for bulges and disks separately. Although the scatter in colour is large, classical bulges lie on the red sequence. The large scatter, especially toward redder colours, is probably due to the difficulty in fitting the linearly scaled B+D model in the g and i-bands. The scatter is similar if we use $r - i$ for the colour. The lower panel in this figure shows the disk components. Disks around any type of bulge have significant overlap in colour. Disks around classical bulges are redder than bulge-less and pseudo-bulge galaxies, in agreement with observations that bulge and disk colour are correlated (de Jong 1994; Peletier & Balcells 1996; Wyse et al. 1997; Cameron et al. 2009).

Using our sample of fitted galaxies, we can examine the morphological properties of $z \approx 0$ galaxies as a function of position in the colour magnitude distribution (CMD). Figure 33 shows the colour magnitude diagram for our sample divided into absolute magnitude bins. Following Mendez et al. (2011); Baldry et al. (2004); Strateva et al. (2001), we fit each magnitude bin with a double Gaussian, and then fit the red sequence by fitting a line to the red peaks of the
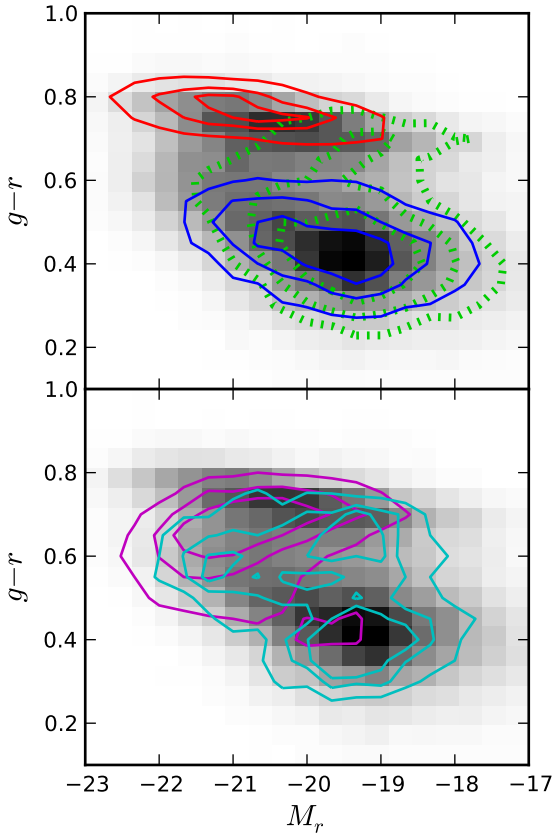
Figure 31. Colour magnitude diagram for different categories in the sample. The underlying grayscale is for the whole sample, using the assigned category to derive magnitudes and colours. In the top panel, the blue contours are the galaxies fit with a single exponential disk and the red contours are the galaxies fit with a single de Vaucouleurs profile. The green, dotted contours show the galaxies fit with a single Sérsic profile. In the lower panel, the cyan contours are the $n_b = 1$ B+D galaxies and the magenta contours are the $n_b = 4$ B+D galaxies. The contours enclose 25%, 50%, and 75% of each category. The colours and magnitudes are corrected using the corrections in §5.3.

double Gaussians. We define the center of the green valley as a line parallel to the red sequence that goes through the minimum of the CMD between $-20 < M_r \leqslant -18.5$. The equation for this line is $(g - r) = -0.025(M_r + 20) + 0.611$. The width of the green valley is taken to be 0.1 in $g - r$, following Mendez et al. (2011). Using this definition of the green valley, and restricting our sample to 69, 666 galaxies with $-23 < M_r < -17$, we find 56%(38, 673) of our sample is blue, 17%(11600) green, and 28%(19, 393) is red. Galaxies with Sérsic fits make up 44%(17, 156), 32%(3, 734), and 20%(3, 971) of the blue, green, and red galaxies, respectively. Ignoring these galaxies, the median B/T for blue, green, and red galaxies is 0.00, 0.27, and 1.0, respectively.

Unsurprisingly, 87%(12, 738) of the exponential disk galaxies fall in the blue cloud, and 94%(9, 086) of the de Vaucouleurs profile-fitted galaxies are red (this is expected due to our selection criteria for ellipticals, see Figure 31). The bulge+disk galaxies span a wider colour distribution (Figure 31). The fractions of $n_b = 4$ B+D galaxies which are blue, green, and red are 34%(4, 805), 31%(4, 337), and 35%(4869).
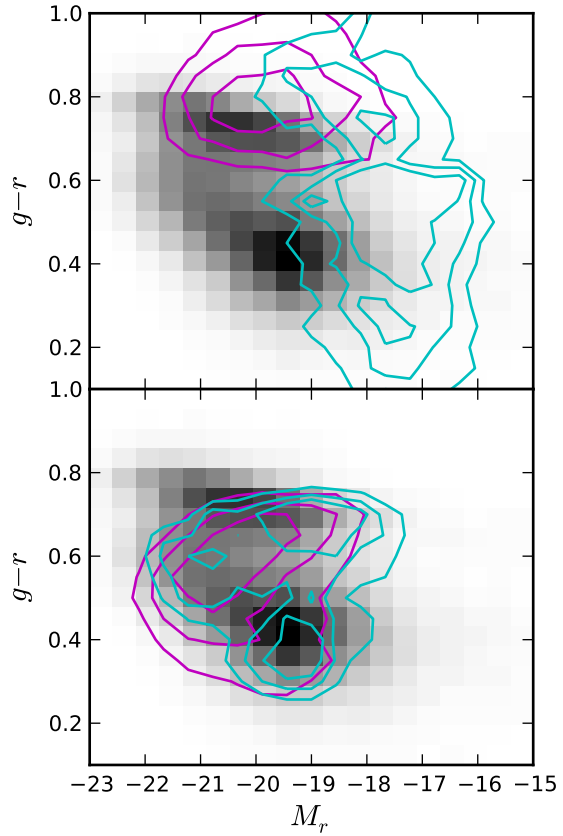

Figure 32. Colour magnitude diagram for bulges(top) and disks(bottom). The underlying grayscale is the CMD for the whole sample; the bulges and disks have been corrected for inclination. The cyan contours are the $n_b = 1$ B+D galaxies, and the magenta countours are the $n_b = 4$ B+D galaxies. The contours enclose 25%, 50%, and 75% of each category.
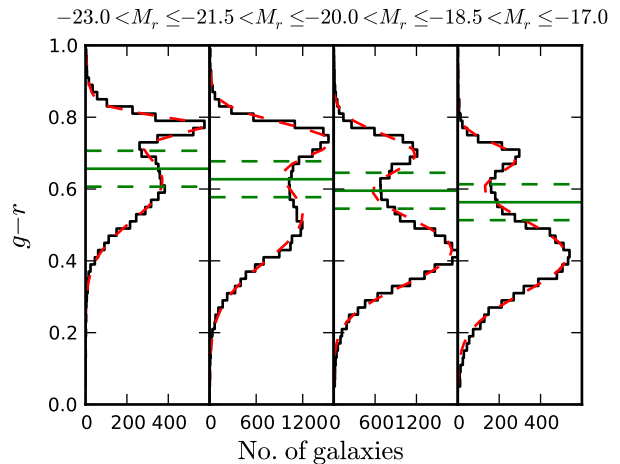

Figure 33. Colour histograms binned by absolute magnitude. The red dashed curve shows a double Gaussian fit to the histogram. The green solid and green dashed lines show the center and limits of the green valley as defined in §5.6.
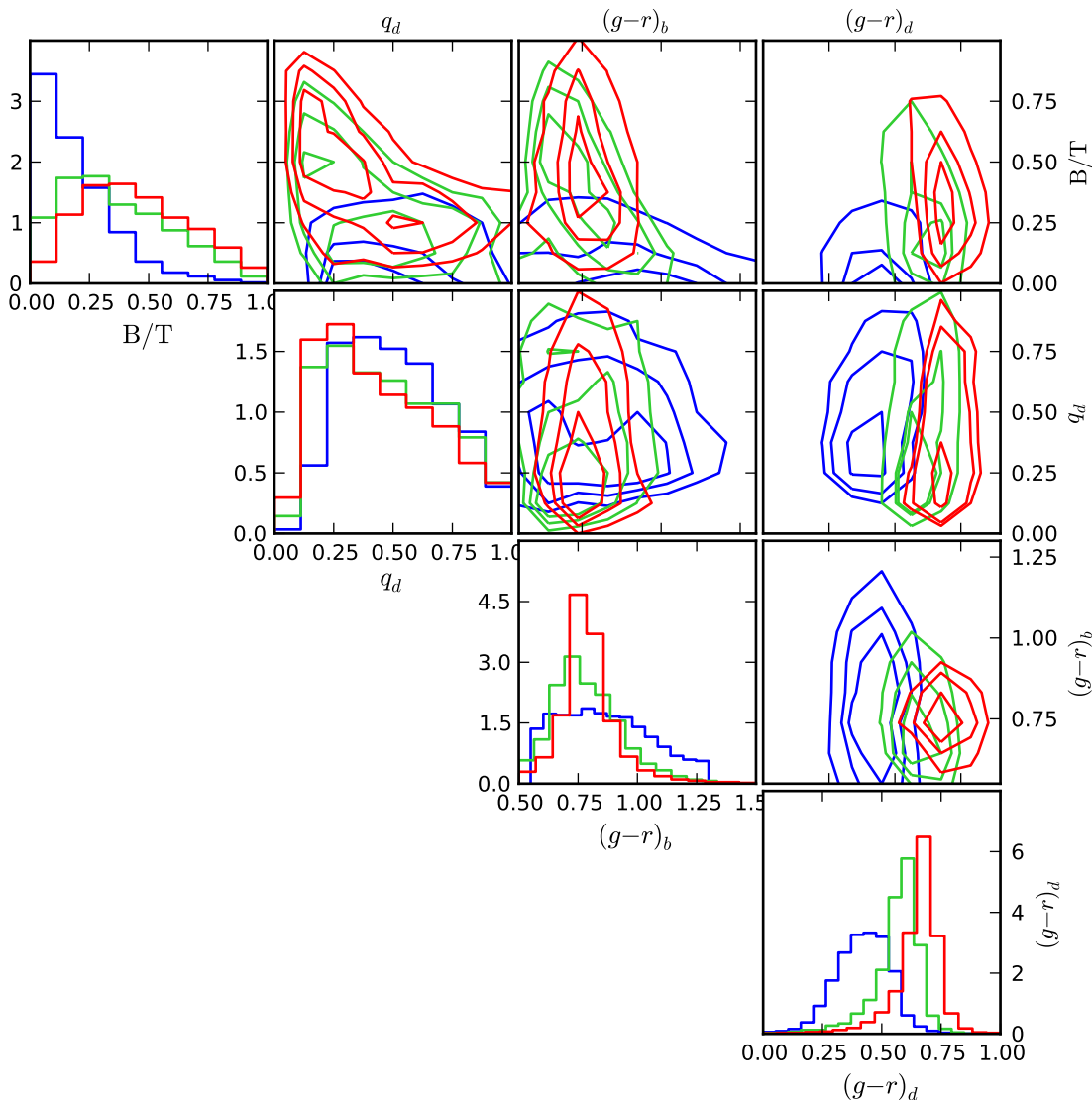
Figure 34. Properties of blue, green, and red B+D galaxies. The columns(rows) are: B/T, disk axis ratio, disk colour, and bulge colour. All quantities are corrected for inclination. The histograms are normalised to aid in the comparison of the different colours. There are 8657 blue galaxies, 5899 green, and 5956 red galaxies. The galaxies are modeled with an $n_b = 4$ B+D or an $n_b = 1$ B+D according to the criteria in §5.1. However, the results do not change if only $n_b = 1$ or only $n_b = 4$ B+D models are used.

For the $n_b = 1$ galaxies the same fractions are 59%(3852), 24%(1562), and 17%(1087). Taken together, the B+D modeled galaxies dominate the green valley (see Figure 31). If we examine only galaxies with good B+D fits, we can separate them by colour into blue, green, and red and examine their properties. This is shown in Figure 34 . Here, we have included all B+D modeled galaxies, with their bulge profile selected as in §5.1. However, the general trends remain the same if we fit all the bulges with either an $n_b = 1$ or $n_b = 4$ Sérsic profile. The rightmost column in Figure 34 shows the distributions of (inclination-corrected) disk colours for the blue, green and red galaxies. Of the properties plotted, the disk colour changes the most as galaxies move from blue to red. The inclination-corrected B/T is shown in the top row. The blue galaxies have smaller bulges with a median B/T of 0.15, while the green and red galaxies have larger bulges,

with median values of 0.33 and 0.42. The median disk colours of blue, green, and red galaxies are 0.43, 0.58, and 0.67, respectively. The fact that a substantial number of galaxies on the red sequence remain disk dominated is in agreement with recent other observations (Bundy et al. 2006, 2010). It suggests that galaxies transitioning to the red sequence may do so through a combination of bulge growth (mergers) and disk fading.

6   SUMMARY

We present a set of 2-dimensional bulge+disk models for $71,825$ nearby ($0.003 < z < 0.05$) SDSS galaxies. We have fit 5 different models to each of the galaxies: an exponential profile, a de Vaucouleurs profile, a Sérsic profile, a de

Vaucouleurs bulge plus exponential disk, and and exponential bulge plus exponential disk. Our models keep the bulge Sérsic index fixed in order to limit the number of free parameters. By fitting classical bulges and ellipticals with de Vaucouleurs profiles, we can more easily facilitate comparisons between their properties. In order to obtain colours, we linearly scale each component of the r-band model in g and i. We have chosen to use r band SDSS images for the fitting, but have shown that these results are consistent to $\sim 10\%$ with those found in g and i band. Our single component fits are in good agreement with the single component fits from SDSS and Blanton et al. (2005). We compare our 2-component fits to G09 and find our models produce similar disk parameters, but that our bulges are typically larger and brighter due to the inclusion of a free Sérsic index and a bar in the G09 models. Nonetheless, our values for B/T and their values for B+Bar/T are comparable.

We examine the systematic and statistical errors in our fits by examining the properties of fits to mock image and fits to a set of 39 bright galaxies from our sample. For both sets of images, we have independently varied the resolution and the S/N. We first examined single component Sérsic fits. For galaxies with high Sérsic indices, the value of $R_{\rm eff}$ decreases(increases) with decreasing resolution(S/N). The opposite occurs for galaxies with low Sérsic indices. Furthermore, the measured Sérsic index is also sensitive to the resolution and S/N; it decreases (especially for high-n galaxies) as galaxies are moved to higher redshift. For single-component fits, the fractional error in $R_{\rm eff}$ is approximately $1.5\times$ as large as the error in the flux for images with $R_{\rm eff}/$PSF FWHM $\gtrsim 0.5$. The relative fractional error in $R_{\rm eff}$ grows rapidly for smaller galaxies, suggesting that 0.5 FWHM is a reasonable lower limit on $R_{\rm eff}$ for a reliable fit. For 2-component fits, there are no clear trends in the fit parameters with decreasing S/N and resolution. Generally, the disk parameters are more robust than the bulge parameters, and the measured B/T increases with redshift for $n_b = 1$ B+D models. However, we do not find that these trends are robust or significant enough to justify adjusting the fits of high-z galaxies to make them comparable to fits of low-z galaxies.

Since each galaxy is fit with 5 different models, we create an algorithm for selecting the preferred model for a given galaxy. Although this algorithm takes into account the χ^2 values for each model, it relies mainly on astrophysically motivated constraints. A galaxy will be fit with a B+D model, if the following are true: the two component fit is a statistically significant improvement over any single component fit; the bulge flux and disk fluxes are nonzero in the linearly-scaled models in g and i-bands; the bulge scale length is smaller than the disk scale length; and the bulge flux dominates in the center of the galaxy. These requirements are satisfied for 29% of our sample. The remainder of the galaxies are fit with a single component exponential (23%), de Vaucouleurs (13%), or Sérsic profile (36%). The last category includes the (intrinsically) faintest galaxies in the sample as well as irregular galaxies, strongly barred galaxies and galaxies with otherwise poor model fits. The fact that the fraction of Sérsic-modeled galaxies as a function of absolute magnitude is independent of the apparent magnitude limit of the sample, demonstrates the robustness of our fitter and

our categorization algorithm; the fits and categorizations are not strongly magnitude-limited in our sample.

In order to distinguish between classical bulges ($n_b = 4$) and pseudo-bulges ($n_b = 1$), we have relied on the colour and flatness of the bulge. We select classical bulges to lie on the red sequence ($g-r > 0.6$). We have not used χ^2 values for the two different B+D models because they are only significantly different for $\sim 5\%$ of all the galaxies. This leaves a sample of 14042 classical bulges and 6684 pseudo-bulges. This division of bulges by colour is a division based on the current star formation occurring in those bulges. We also examine the Kormendy relation for bulges and ellipticals and show that the majority of classical bulges lie along to the elliptical galaxy Kormendy relation, while the pseudo-bulges do not. This supports the use of colour as a division between the two dynamically different bulges.

Given our sample of B+D galaxies, we examine their properties as a function of total galaxy colour. We find that classical bulge galaxies are evenly distributed among red, green, and blue while pseudo-bulge galaxies are predominately blue, but both types are a significant fraction of green valley galaxies (70% for galaxies brighter than 16 in r). Furthermore, the difference between red and green B+D galaxies is predominately due to the disk becoming redder, not growth of the central bulge.

This work presents a large, homogeneous sample of B+D galaxies to date. Nonetheless, it is evident from our S/N and resolution tests, that there are serious limitations to the quality of B+D fits from ground-based data. In classifying our fits, we have tried to be conservative, only using a B+D where it makes statistical and astrophysical sense. Despite these limitations, the size of our sample allows us to create large subsamples of galaxies of different morphological types. In future works, we plan to examine the mass fractions of bulges (and ellipticals) and disks, at least for massive galaxies where the contribution from Sérsic-modeled galaxies is small. We also plan to examine single morphological types in greater detail. For example, we have found $\sim 14,000$ galaxies with robust classical bulges, which span a wide range of B/T, luminosity(mass), stellar age, and environment. Because the sample is large, we can examine correlations between environment and classical bulge properties and attempt to answer questions about bulge (and disk) formation, in a statistically meaningful way.

Group, the Instituto de Astrofisica de Canarias, the Michigan State/Notre Dame/JINA Participation Group, Johns Hopkins University, Lawrence Berkeley National Laboratory, Max Planck Institute for Astrophysics, New Mexico State University, New York University, Ohio State University, Pennsylvania State University, University of Portsmouth, Princeton University, the Spanish Participation Group, University of Tokyo, University of Utah, Vanderbilt University, University of Virginia, University of Washington, and Yale University.

REFERENCES

Abazajian K. N., Adelman-McCarthy J. K., et al., 2009, ApJS, 182, 543

Aihara H., Allende Prieto C., An D., et al., 2011, ApJS, 193, 29

Allen P. D., Driver S. P., Graham A. W., et al., 2006, MNRAS, 371, 2

Athanassoula E., 2005, MNRAS, 358, 1477

Balcells M., Graham A. W., et al., 2003, ApJ, 582, L79

Baldry I. K., Glazebrook K., Brinkmann J., et al., 2004, ApJ, 600, 681

Bamford S. P., Nichol R. C., Baldry I. K., et al., 2009, MNRAS, 393, 1324

Bell E. F., Wolf C., Meisenheimer K., et al., 2004, ApJ, 608, 752

Benson A. J., Džanović D., Frenk C. S., Sharples R., 2007, MNRAS, 379, 841

Bernardi M., Hyde J. B., Sheth R. K., Miller C. J., Nichol R. C., 2007, AJ, 133, 1741

Bernardi M., Sheth R. K., Annis J., et al., 2003, AJ, 125, 1849

Blanton M. R., Eisenstein D., Hogg D. W., et al., 2005, ApJ, 629, 143

Blanton M. R., Hogg D. W., Bahcall N. A., Baldry I. K., et al., 2003, ApJ, 594, 186

Blanton M. R., Roweis S., 2007, AJ, 133, 734

Blanton M. R., Schlegel D. J., Strauss M. A., et al., 2005, AJ, 129, 2562

Bundy K., Ellis R. S., Conselice C. J., et al., 2006, ApJ, 651, 120

Bundy K., Scarlata C., Carollo C. M., Ellis R. S., et al., 2010, ApJ, 719, 1969

Burstein D., Haynes M. P., Faber M., 1991, Nat, 353, 515

Cameron E., Driver S. P., Graham A. W., Liske J., 2009, ApJ, 699, 105

Caon N., Capaccioli M., D'Onofrio M., 1993, MNRAS, 265, 1013

Capaccioli M., Held E. V., Nieto J.-L., 1987, AJ, 94, 1519

de Jong R. S., 1994, PhD thesis, , Kapteyn Astronomical Inst., (1994)

de Jong R. S., 1996, A&AS, 118, 557

de Souza R. E., Gadotti D. A., dos Anjos S., 2004, ApJS, 153, 411

de Vaucouleurs G., 1948, Annales d'Astrophysique, 11, 247

de Vaucouleurs G., 1959, Handbuch der Physik, 53, 275

Driver S. P., Allen P. D., Graham A. W., Cameron E., et al., 2006, MNRAS, 368, 414

Driver S. P., Popescu C. C., Tuffs R. J., et al., 2007, MNRAS, 379, 1022

Driver S. P., Popescu C. C., Tuffs R. J., et al., 2008, ApJ, 678, L101

Drory N., Fisher D. B., 2007, ApJ, 664, 640

Eggen O. J., Lynden-Bell D., Sandage A. R., 1962, ApJ, 136, 748

Elmegreen B. G., Bournaud F., Elmegreen D. M., 2008, ApJ, 688, 67

Falcón-Barroso J., Peletier R. F., et al., 2002, MNRAS, 335, 741

Fathi K., Peletier R. F., 2003, A&A, 407, 61

Fisher D. B., 2006, ApJ, 642, L17

Fisher D. B., Drory N., 2008, AJ, 136, 773

Franx M., Illingworth G., Heckman T., 1989, AJ, 98, 538

Freeman K. C., 1970, Astrophysical Journal, 160, 811

Gadotti D. A., 2008, MNRAS, 384, 420

Gadotti D. A., 2009, MNRAS, 393, 1531

Gonzalez A. H., Zabludoff A. I., Zaritsky D., 2005, ApJ, 618, 195

Graham A. W., 2001, AJ, 121, 820

Graham A. W., Worley C. C., 2008, MNRAS, 388, 1708

Guo Y., McIntosh D. H., Mo H. J., et al., 2009, MNRAS, 398, 1129

Hao L., Strauss M. A., Fan X., Tremonti C. A., et al., 2005, AJ, 129, 1795

Hao L., Strauss M. A., Tremonti C. A., Schlegel D. J., et al., 2005, AJ, 129, 1783

Hubble E. P., 1936, Realm of the Nebulae

Jarrett T. H., Chester T., Cutri R., Schneider S., et al., 2000, AJ, 119, 2498

Kauffmann G., Heckman T. M., Tremonti C., et al., 2003, MNRAS, 346, 1055

Kent S. M., 1985, ApJS, 59, 115

Kent S. M., 1986, AJ, 91, 1301

Kormendy J., 1977, ApJ, 218, 333

Kormendy J., 1993, in H. Dejonghe & H. J. Habing ed., Galactic Bulges Vol. 153 of IAU Symposium, Kinematics of extragalactic bulges: evidence that some bulges are really disks. pp 209–+

Kormendy J., Kennicutt Jr. R. C., 2004, ARA&A, 42, 603

Kregel M., van der Kruit P. C., de Grijs R., 2002, MNRAS, 334, 646

Lauer T. R., Faber S. M., Richstone D., et al., 2007, ApJ, 662, 808

Laurikainen E., Salo H., Buta R., et al., 2010, MNRAS, 405, 1089

Lima Neto G. B., Gerbal D., Márquez I., 1999, MNRAS, 309, 481

Liske J., Lemon D. J., Driver S. P., Cross N. J. G., Couch W. J., 2003, MNRAS, 344, 307

Lupton R., 1993, Statistics in theory and practice

MacArthur L. A., Ellis R. S., Treu T., et al., 2008, ApJ, 680, 70

Maller A. H., Berlind A. A., Blanton M. R., Hogg D. W., 2009, ApJ, 691, 394

Mandelbaum R., Hirata C. M., Seljak U., et al., 2005, MNRAS, 361, 1287

Markwardt C. B., 2009, in D. A. Bohlender, D. Durand, & P. Dowler ed., Astronomical Society of the Pacific Conference Series Vol. 411 of Astronomical Society of the Pacific Conference Series, Non-linear Least-squares Fitting in IDL with MPFIT. pp 251–+

Masters K. L., Mosleh M., Romer A. K., Nichol R. C.,

Bamford S. P., Schawinski K., Lintott C. J., Andreescu D., Campbell H. C., Crowcroft B., Doyle I., Edmondson E. M., Murray P., Raddick M. J., Slosar A., Szalay A. S., Vandenberg J., 2010, MNRAS, 405, 783

Mendez A. J., Coil A. L., Lotz J., et al., 2011, ArXiv e-prints

Moorthy B. K., Holtzman J. A., 2006, MNRAS, 371, 583

Noguchi M., 1999, ApJ, 514, 77

Padmanabhan N., Schlegel D. J., Finkbeiner D. P., et al., 2008, ApJ, 674, 1217

Peletier R. F., Balcells M. D. R. L., et al., 1999, MNRAS, 310, 703

Peletier R. F., Balcells M., 1996, AJ, 111, 2238

Peng C. Y., Ho L. C., Impey C. D., Rix H., 2002, AJ, 124, 266

Sandage A., 1961, The Hubble atlas of galaxies

Schawinski K., Lintott C., Thomas D., et al., 2009, MNRAS, 396, 818

Sersic J. L., 1968, Atlas de galaxias australes. Cordoba, Argentina: Observatorio Astronomico, 1968

Shao Z., Xiao Q., Shen S., Mo H. J., et al., 2007, ApJ, 659, 1159

Simard L., Mendel J. T., Patton D. R., Ellison S. L., McConnachie A. W., 2011, ApJS, 196, 11

Simard L., Willmer C. N. A., Vogt N. P., Sarajedini V. L., et al., 2002, ApJS, 142, 1

Simmons B. D., Urry C. M., 2008, ApJ, 683, 644

Strateva I., Ivezić Ž., Knapp G. R., et al., 2001, AJ, 122, 1861

Trujillo I., Graham A. W., Caon N., 2001, MNRAS, 326, 869

Tully R. B., Pierce M. J., Huang J.-S., et al., 1998, AJ, 115, 2264

van den Bergh S., 2009, ApJ, 702, 1502

Weinzirl T., Jogee S., Khochfar S., et al., 2009, ApJ, 696, 411

Wyse R. F. G., Gilmore G., Franx M., 1997, ARA&A, 35, 637